

Learning to design drug-like molecules in three-dimensional space using deep generative models

Yibo Li,[†] Jianfeng Pei,^{*,‡} and Luhua Lai^{*,†,‡,¶}

[†] *Center for Life Sciences, Academy for Advanced Interdisciplinary Studies, Peking University, Beijing 100871, China*

[‡] *Center for Quantitative Biology, Academy for Advanced Interdisciplinary Studies, Peking University, Beijing 100871, China*

[¶] *BNLMS, State Key Laboratory for Structural Chemistry of Unstable and Stable Species, College of Chemistry and Molecular Engineering, Peking University, Beijing 100871, China*

E-mail: jfpei@pku.edu.cn; lhlai@pku.edu.cn

Abstract

Recently, deep generative models for molecular graphs are gaining more and more attention in the field of *de novo* drug design. A variety of models have been developed to generate topological structures of drug-like molecules, but explorations in generating three-dimensional structures are still limited. Existing methods have either focused on low molecular weight compounds without considering drug-likeness or generate 3D structures indirectly using atom density maps. In this work, we introduce Ligand Neural Network (L-Net), a novel graph generative model for designing drug-like molecules with high-quality 3D structures. L-Net directly outputs the topological and 3D structure of molecules (including hydrogen atoms), without the need for additional atom placement or bond order inference algorithm. The architecture of L-Net is specifically optimized

for drug-like molecules, and a set of metrics is assembled to comprehensively evaluate its performance. The results show that L-Net is capable of generating chemically correct, conformationally valid molecules with high drug-likeness. Finally, to demonstrate its potential in structure-based molecular design, we combine L-Net with MCTS and test its ability to generate potential inhibitors targeting ABL1 kinase.

1 Introduction

The search for molecules with good bioactivity and druggability is the central task of *de novo* drug discovery, which is complicated by the enormous size and complexity of the chemical space.¹ To facilitate the search for novel molecular structures, a variety of computational *de novo* molecular design algorithms²⁻⁴ have been developed aiming to make the exploration of chemical space more efficient. However, classical *de novo* design algorithms require expert-crafted rules to guarantee that the output molecule is practical, and usually requires extensive tuning of parameters in the scoring function or optimization algorithms to achieve good performance.

With the popularization of deep learning techniques, there is a growing interest in applying deep generative models to the problem of *de novo* molecule design. Deep neural networks are highly expressive and generalizable and can be trained in a fully data-driven manner, with minimum requirements for expert knowledge. Early works have utilized SMILES-based generative models for molecule generation,^{5,6} while more recent models have enabled the direct generation of molecular graphs using graph convolutional neural network.⁷⁻⁹ Those methods have demonstrated promising performance in a variety of molecular design tasks, including generation based on scaffold,¹⁰ pharmacophore¹¹ and targets.⁷

Most of the existing works in this field have focused on generating 2D (or topological) structures based on 2D conditions. However, 3D information is highly important for designing molecules with high bio-activity. For example, protein structures are routinely used in docking studies for structure-based drug discovery (SBDD), and ligand information can

be used to build 3D-QSAR models for activity prediction. It is therefore highly desirable to include 3D condition into deep generative models for molecules, but explorations in this direction have been rather limited, and there are still many problems needs to be solved.

One way to incorporate 3D information is to condition the existing SMILES-based generative models on 3D data, such as molecular shape¹² and pocket structure.¹³ Those methods have demonstrated effectiveness in ligand and structure-based drug discovery. However, the output molecules by those models do not contain 3D information, and an additional optimization step is usually required to embed them into 3D space. A more desirable approach is to directly generate 3D coordinates, as done previously by Gebauer et al.,¹⁴ Sim et al.¹⁵ and Nesterov et al.¹⁶ However, these methods mainly focused on structurally simple molecules such as those in the QM9 dataset, and their applicability to drug-like molecules is currently unclear. On the other hand, more recent work by Ragoza et al.¹⁷ has placed focus on drug-like molecules. Their model works by first generating the atomic density map, converting it to atomic positions, and finally converting those spatial points into molecular structures. However, it is not an end-to-end method and requires multiple components, both deep learning-based and rule-based, to work together to generate the final molecule output.

In this work, we develop a novel deep learning model for the end-to-end generation of drug-like molecules with high-quality 3D structures. The model builds molecule iteratively by adding new atoms and bonds to the existing structure step-by-step and outputs results with full 3D coordinates, without the need for additional processing steps. To achieve good performance in generating conformationally valid molecules, a new network architecture, named L-Net (which stands for “ligand neural network”), is proposed. We design the network to be covariant against rotation and translation, and domain knowledge is incorporated into the network to improve the chemical validity of the generated molecules. We show that our proposed method is capable of generating chemically correct, conformationally valid, and highly drug-like molecules. Finally, in order to demonstrate its potential application in SBDD, we combine the model with Monte Carlo tree search (MCTS), a widely applied

technique in reinforcement learning, and use it to optimize molecules targeting ABL1. To our knowledge, this work presents the first attempt to apply an autoregressive 3D graph generative model to an SBDD problem. The major contributions of this paper are summarized as follows:

- We propose a new 3D molecule generative model called L-Net that is specifically designed to generate drug-like molecules.
- We assemble a set of evaluation metrics to comprehensively measure the performance of the proposed model. Compared with previous benchmarks for 2D models, the proposed metrics emphasize the quality of 3D structures.
- As a proof of concept, we combine L-Net with MCTS to design potential inhibitors against ABL1.

2 Methods

2.1 The molecule generation process

The task of our generative model is to produce molecular graphs $G = (V, E, A, B, X)$, where V is the set of nodes (atoms), E is the set of edges (bonds), $A = \{a_v\}_{v \in V}$ are the atom type labels, $B = \{b_{uv}\}_{(u,v) \in E}$ are bond type labels, and $X = \{\mathbf{x}_v\}_{v \in V}$ are the 3D positions of each atoms. Note that in theory, the bond order can be inferred directly from distances between atoms, as done in several previous works,^{14,17} but existing bond type assignment algorithms are generally sensitive to errors, even small ones that can be later corrected. To make our model more robust, we explicitly output the bond types B .

Our proposed model generates the graph in a step-by-step manner. More specifically, the model generates a molecular graph by iteratively building its spanning tree. A spanning tree of G is a tree structure that contains all nodes in G (see Figure 1a). Tree-based structures are much simpler than general unconditional graphs, and its generation is more straightforward

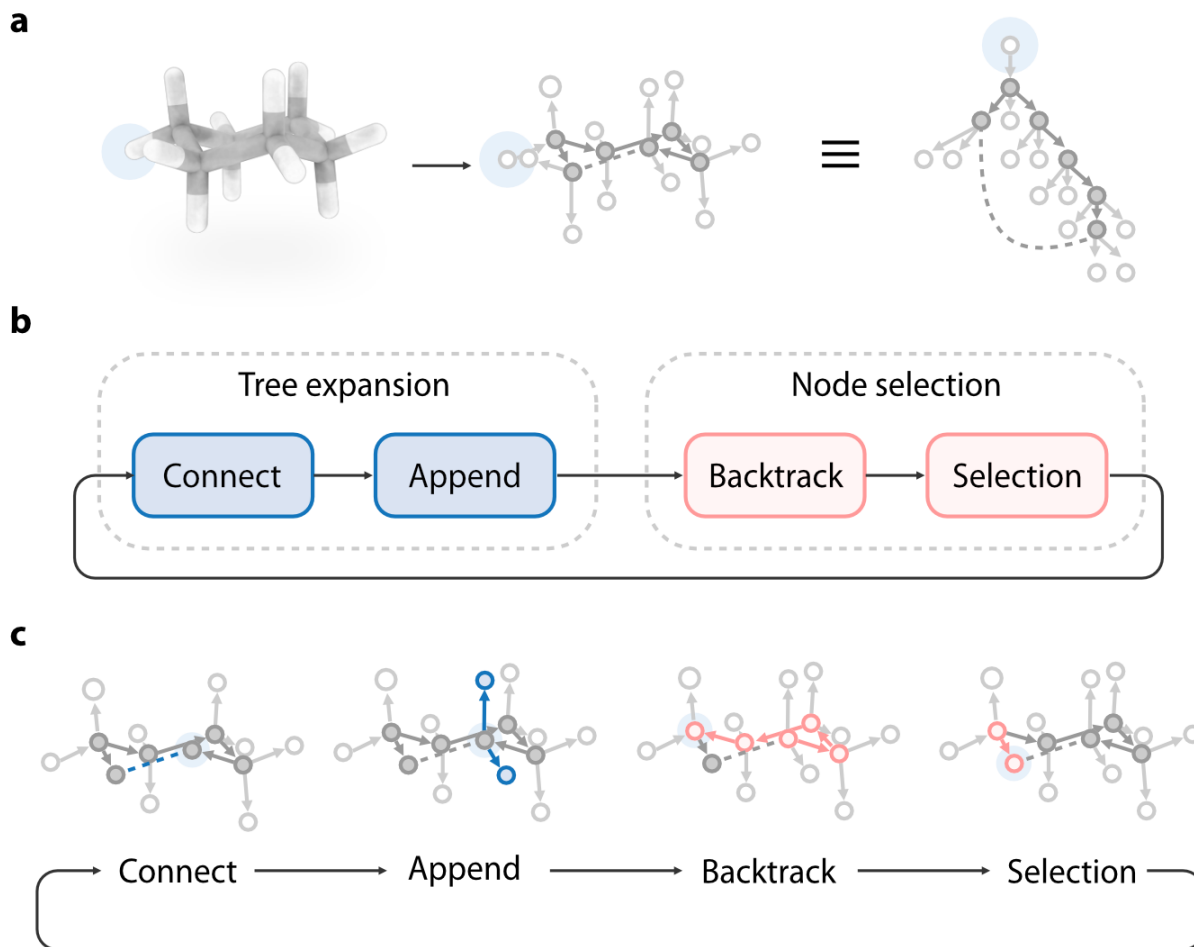


Figure 1: The molecule generation process, using cyclohexane as an example: **a**. The model generates a molecule by generating its spanning tree in a depth-first manner. The root of the tree is highlighted in light blue; **b**. The model builds the spanning tree iteratively, and two sub-steps are performed at each iteration: tree expansion and node selection. At the tree expansion step, the model connects the currently focused atom with another atom (the “connect” operations), or add new atoms to the focused atom (the “append” operations). At the node selection step, the model backtracks the spanning tree to find the next focus atom (the “backtrack” and “selection” operations); **d**. An example showing a few steps during the generation of cyclohexane. Blue atoms or bonds indicates newly added structures during the tree expansion step. Pink arrows indicate the process of finding the next focused atom. The focused atom at each step is highlighted using a light blue circle.

using a depth-first approach. At each iteration, the following two steps are performed to build the spanning tree (Figure 1**b**):

- Node selection: The model selects a “focus atom” from the set of suitable atoms that

have already been generated. An atom is suitable for becoming a focused atom if it has unfilled valences (as an example, see the focused atom in Figure 1c);

- Tree expansion: The model performs edits around the focused atom, by either adding new atoms to it (the “append” operation) or by connecting it with another existing atom (the “connect” operation).

During the “node selection” step, the model searches through the spanning tree to find the next focused atom:

- If the currently focused atom has a child atom whose valence has not been filled, the model will select that atom to be the next focus. If multiple such children exist, a ranking is performed and the highest-ranking child is selected;
- If no such child exists for the current focus, a “backtracking” operation is performed to find an ancestor who has such children. And that child is then selected as the next focus.

This process terminates when there are no atoms suitable for becoming the “focused atom”, that is, the valences of all atoms have been filled. During the generation process, there are a variety of decisions that needs to be made by the model:

- During the “connect” operation, the model needs to decide which atom to connect with, using what type of bond;
- During the “append” operation, the model needs to decide how many atoms should be added to the graph, their atom type, 3D location, and the type of bonds connecting them to the focused atom.
- The model also needs to output the ranking of each atom, which will be used in the node selection step.

Those decisions are all made using a neural network with a novel architecture we called L-Net. L-Net is composed of two parts: The first part is a state encoder, which maps the intermediate molecular structure G_i at step i into a continuous representation $\mathbf{h}_i = f_\theta(G_i)$. The second part is a policy network, which assign a probability value to each available action based on the current state $p_\theta(a|\mathbf{h}_i)$. The architecture of L-Net is explained in detail from Section 2.2 though 2.5. To make the network capable of generating drug-like molecules, we construct a drug-like subset of the ChEMBL dataset¹⁸ and created an ‘‘expert trajectory’’ for generating each molecule in the dataset. L-Net is then trained by imitating those trajectories. Data collection and preprocessing workflows are given in Section 2.7, and the training details are given in Section 2.8. Finally, to validate the model’s performance, we designed a set of evaluation metrics which are discussed in Section 2.11.

2.2 The architecture of the state encoder

At iteration i , the state encoder of L-Net is responsible for mapping the current molecular graph G_i to continuous representations $h_i = (\mathbf{h}_{i,g}, \{\mathbf{h}_{i,v}\}_{v \in V_i}) = f_\theta(G_i)$, where $\mathbf{h}_{i,g}$ is the graph level representation, and $\{\mathbf{h}_{i,v}\}_{v \in V_i}$ are atom level representations. The architecture of f_θ is shown in Figure 2. The network adopts a U-net structure.¹⁹ The input is first fed into an embedding layer to create the input representation for atoms and bonds. It is then passed into the U-net, which is built from convolutional layers, pooling layers, and unpooling layers. The convolutional layers adopt the architecture of MPNN,²⁰ and are organized into DenseNet blocks²¹ to improve the performance. Pooling layers and unpooling layers use a node clustering method that is specifically designed for this use-case. The results are collected and fed to the policy network.

The following sections are devoted to giving detailed explanations of the individual components of the state encoder. We first describe the embedding layer in Section 2.3, and then graph convolution layer in Section 2.4. Pooling and unpooling layers, as well as the node clustering algorithm, are discussed in Section 2.5.

2.3 The embedding layers

2.3.1 Embeddings of atom and bond types

The embeddings of atom and bond types are created by indexing through a trainable lookup table. The dimensionality of those embeddings is 2. Note that the atom type of a node v is defined by a tuple of three variables $a_v = (a_v^e, a_v^c, a_v^f)$: the element type a_v^e , formal charge a_v^c , and whether the atom is the focused atom a_v^f . Each of those variables is embedded separately and then concatenated together. We also add “temporal encodings” to each atom to record the time that atom is added to the graph, similar to what is done by Vaswani et al.:²²

$$\mathbf{h}_v^{\sin} = \left[\sin \frac{t_v}{T^{2l/d_{\text{model}}}} \right]_{l=1}^{d_{\text{model}}/2}$$

$$\mathbf{h}_v^{\cos} = \left[\cos \frac{t_v}{T^{2l/d_{\text{model}}}} \right]_{l=1}^{d_{\text{model}}/2}$$

Where t_v is the step when the atom v is added to the graph, d_{model} is the size of the temporal embedding, l is the indices of the temporal embedding, T determines the maximum wavelength of the sine and cosine embedding function, $[\cdot; \cdot]$ means the vertical concatenation of vectors. In this work, $d_{\text{model}} = 40$, $T = 30$. Those vectors are then projected into a vector of size 3 with a linear layer without activation.

Local coordinate system and rotational covariance Besides type information, the position of each atom should also be included in the input. Ideally, this should be done in a rotationally and translationally covariant way. More specifically, our model parametrize a probability distribution (called the “policy”) in 3D space $p(\mathbf{x}|G)$ to indicate where the new atom should be placed (Figure 3a). If we rotate the existing structure G by a certain amount, the probability distribution $p(\mathbf{x}|G)$ should also be rotated by the same amount (Figure 3b). Mathematically, this is expressed by the equation $p(\mathbf{x}|T(G)) = p(T^{-1}(\mathbf{x})|G)$, where T is an

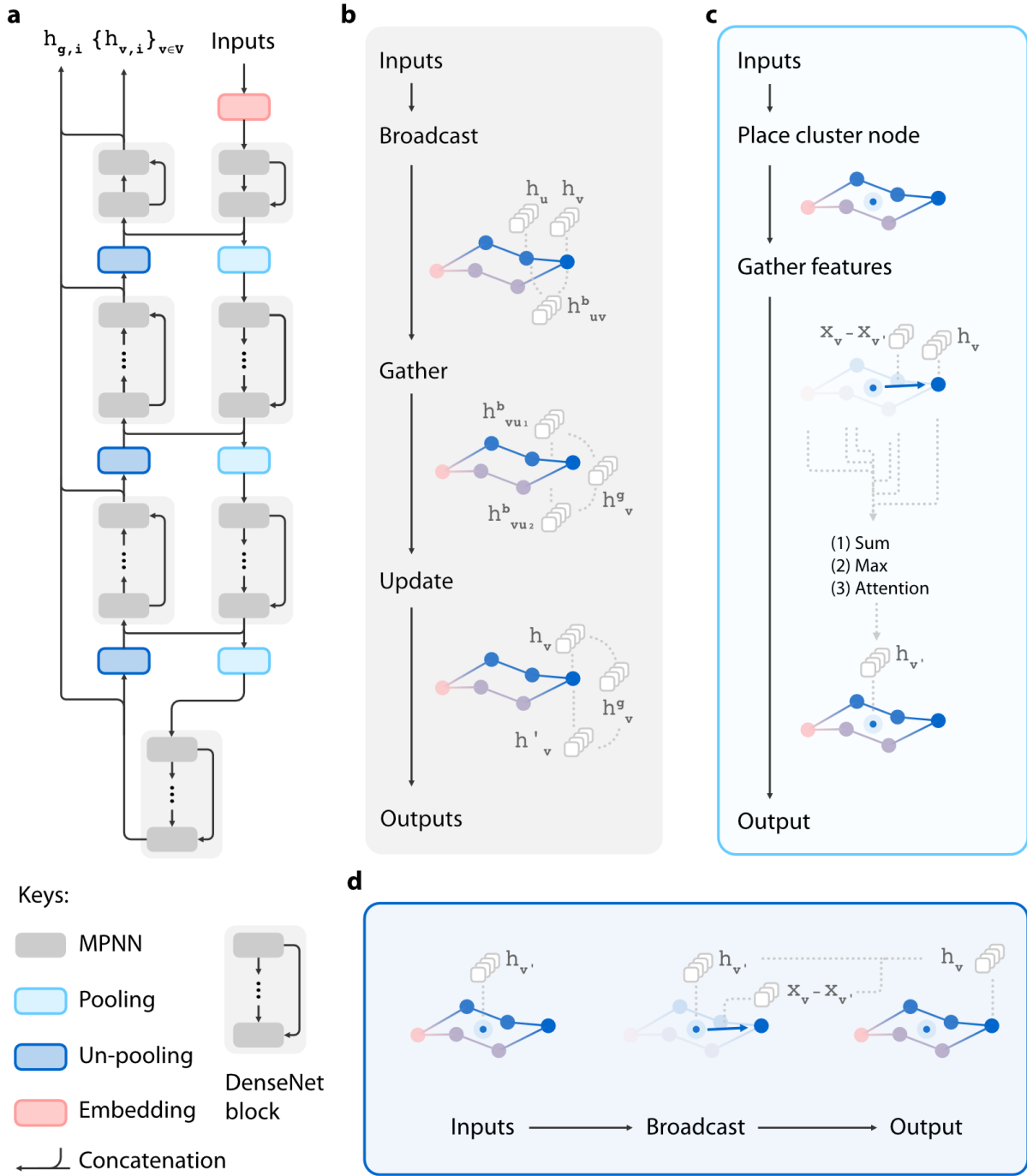


Figure 2: An overview of the architecture for the state encoder. **a**. The overall architecture of the state encoder; **b**. The architecture of each graph convolutional layer; **c**. The architecture of each pooling layer; **d**. The architecture of each unpooling layer.

spatial operation from the special Euclidean group $SE(3)$.

Enforcing rotational covariance into the network is a non-trivial task. Previous works have

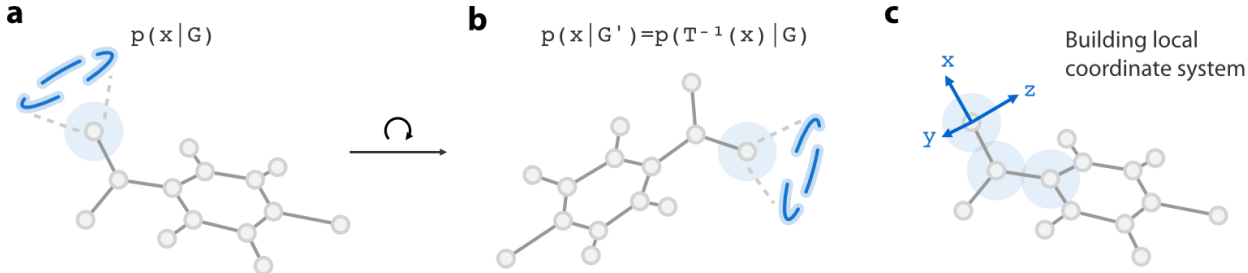


Figure 3: Enforcing rotational covariance using a local coordinate system. An ideal 3D molecule generative model should be rotationally equivariant. If the existing structure is rotated by a certain amount (a), the atom placement policy $p(x|G)$ should also be rotated equivalently (b). We solve this problem by introducing a local coordinate system in the focused atom (c). Since this coordinate system is rotationally covariant, so will the probability distribution defined in the coordinate system.

developed specialized network architectures, such as tensor field network²³ or Cormorant,²⁴ to ensure rotational covariance. Those works are theoretically elegant but are difficult to implement, and their expressiveness may be restricted in some highly symmetrical cases.

Here, we adopt a much simpler yet effective approach, by creating a local coordinate system at the current focus using its neighbor atoms (Figure 3c). We then express the distribution in the local coordinate system $q(\mathbf{x}|G) = p(T(\mathbf{x})|T(G))$, where T indicates the transformation from global to local coordinate. It is easy to verify that q is rotationally covariant, even if p is not, since the local coordinate system is covariant against rotation. Similar methods have been previously used to construct the 3D representation of proteins,²⁵ but to our knowledge, we are the first to use this technique in the generative model of small molecules.

Under this framework, the 3D information feed into the neural network are all under the local coordinate system:

$$\tilde{\mathbf{x}}_v = M(\mathbf{x}_v - \mathbf{x}_{v'})$$

$$\tilde{\mathbf{x}}_{uv} = \tilde{\mathbf{x}}_u - \tilde{\mathbf{x}}_v$$

Where $\tilde{\mathbf{x}}_v$ is the position feature of atom v , $\tilde{\mathbf{x}}_{uv}$ is the position feature of bond uv , and M is the matrix for transforming into the local coordinate system. Those features are projected into a vector of length 8 using a linear layer with no activation.

2.4 Graph convolutional layers

The major components of the state encoder are graph convolutional (GC) layers. The GC architecture used in this work is similar to that used before,¹⁰ with broadcast, gathering and update operations parametrized using linear layers with elu activation function (as shown in Figure 2b). The only difference lies in the gathering operation. Besides summation and maximization, we add attention as an additional reduction method to improve the expressiveness of the model. Also similar to the previous work, we add “virtual” bonds to the graph to increase the size of receptive fields for each GC layer.

The GC layers are organized into multiple DenseNet blocks (as shown in Figure 2). DenseNet is a type of network architecture that aims to increase the performance scalability for deeper networks by introducing short connections between any two layers.²¹ There are three major hyper-parameter for DenseNet: the growth rate, the bottleneck size, and the network depth. We experiment with three configurations of DenseNet architectures:

The standard configuration, with bottleneck size of 94, growth rate of 24, and the depths of DenseNet blocks (in the order of dataflow in U-Net) [2, 4, 6, 8, 6, 4, 2];

The shallow DenseNet, with the same bottleneck size and growth rate as the basic configuration, and change the depth of DenseNet blocks to [2, 2, 4, 6, 4, 2, 2];

The narrow DenseNet, with the depth of each DenseNet block the same as the basic configuration, and the bottleneck size and growth rate reduced to half.

We will show (in Section 3) that reducing the depth or width of the DenseNet blocks will both hurt the model’s performance. Since adding more layers or depth will increase the computational burden, we suggest the use of the “standard” configuration for future adoption of the model.

2.5 Pooling and unpooling operations in graph U-net

U-nets¹⁹ have enjoyed great success in image-related pixel-wise prediction tasks. It can achieve a high receptive field size with fewer layers, while significantly reduced memory consumption during training. The major problem for applying U-net in graph generation is that, unlike images and 3D voxels, there are no canonical ways to perform pooling and unpooling on graphs.²⁶ In order to perform pooling and unpooling on molecular graphs, we designed a custom clustering scheme:

- In the first level of clustering, atoms with one valence, such as hydrogens, halogen, and oxygens in carbonyl groups, are collapsed to their neighbor atoms. For most molecules, almost half of their atoms are hydrogen, consuming a significant amount of GPU memory. This level of clustering enables us to include hydrogens into the generation process in an efficient way, by compressing the information of hydrogens into its neighboring heavy atoms.
- In the second level of clustering, molecules are fragmented into ring assemblies and chains. This method is previously used to define molecule scaffold²⁷ and to organize scaffold datasets.²⁸ After fragmentation, atoms in the same ring assembly or chain are clustered together.
- In the final level of clustering, all nodes are collapsed into a single graph-level master node.

A visual demonstration of this scheme is given in Figure 4. After the clustering method is defined, the pooling and unpooling operations can subsequently be defined, as shown in Figure 2**c,d**. For pooling layers, we first need to define the 3D placement of the cluster node:

$$\Delta \mathbf{x}_v = \text{MLP}_{\text{pooling}}^{\text{displace}}(\mathbf{h}_v)$$

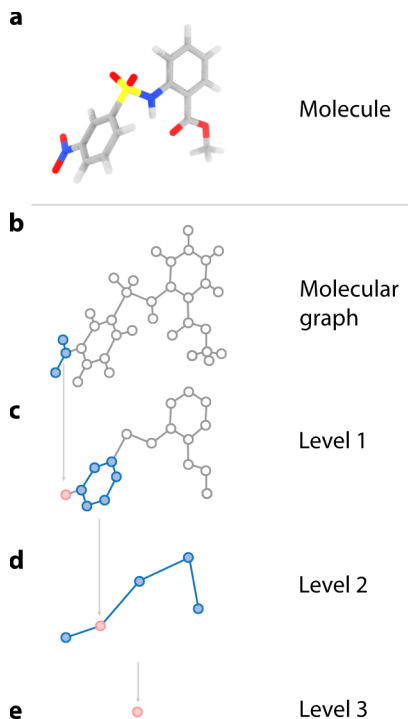


Figure 4: A custom three-level node clustering scheme for pooling and unpooling operations in molecular graphs.

$$\mathbf{x}_{v'} = \frac{1}{|C|} \sum_{v \in C} (\mathbf{x}_v + \Delta \mathbf{x}_v)$$

Where v' is the cluster node, C is the set of nodes clustered v' , and $\text{MLP}_{\text{Pooling}}^{\text{Displace}}$ is a linear layer with elu activation. In other words, we place v' at the geometric center of the nodes to be clustered and displace it with a small deviation (initialized as zeros) calculated using a neural network. After determining the 3D location of v' , the features after pooling is calculated as:

$$\mathbf{h}_{v'}^{\text{sum}} = \sum_{v \in C} \text{MLP}_{\text{pooling}}^{\text{sum}}([\mathbf{h}_v, \mathbf{x}_v - \mathbf{x}_{v'}])$$

$$\mathbf{h}_{v'}^{\text{max}} = \max_{v \in C} \text{MLP}_{\text{pooling}}^{\text{max}}([\mathbf{h}_v, \mathbf{x}_v - \mathbf{x}_{v'}])$$

$$\mathbf{h}_v^{\text{att}}, a_v^{\text{att}} = \text{MLP}_{\text{pooling}}^{\text{att}}([\mathbf{h}_v, \mathbf{x}_v - \mathbf{x}_{v'}])$$

$$\mathbf{h}_{v'}^{\text{att}} = \frac{\sum_{v \in C} \exp a_u^{\text{att}} \mathbf{h}_v^{\text{att}}}{\sum_{v \in C} \exp a_u^{\text{att}}}$$

$$\mathbf{h}_{v'} = [\mathbf{h}_{v'}^{\text{sum}}, \mathbf{h}_{v'}^{\text{max}}, \mathbf{h}_{v'}^{\text{att}}]$$

This may seem complicated first, but it is essentially the process of gathering information using multiple reduction methods, including sum, maximization, and attention, and concatenate the result together. The unpooling layers have a much simpler architecture:

$$\mathbf{h}_v = \text{MLP}_{\text{unpooling}}([\mathbf{h}_{v'}, \mathbf{x}_v - \mathbf{x}_{v'}])$$

Which uses a single fully connected layer to broadcast information to the nodes belonging to the cluster.

2.6 The policy network

After creating a continuous representation of the current state G_i using the state encoder $h_i = (\mathbf{h}_{i,g}, \{\mathbf{h}_{i,v}\}_{v \in V_i}) = f_\theta(G_i)$, the policy network is used to decide what action should be carried out. Recall that there are three types of decision the policy network need to make:

- The type and position of new atoms during the “append” operation;
- The atom to be connected and the type of connecting bond during the “connect” operation;
- The rank of the new atoms to be added.

We denote the policies for each decision as p_θ^{append} , $p_\theta^{\text{connect}}$ and p_θ^{rank} .

Decision making during the “append” operation During the “append” operation, one or more atoms are created and added to the focused atom v' . We represent a newly created atom as the tuple $v^* = (a, b, \mathbf{x})$, where a is the atom type, b is the bond type used to connect the new atom with the focused atom, $\mathbf{x} = (r, \theta, \phi)$ is the spherical coordinate of this new atom in the local coordinate system (described in Section 2.3). The policy network for the append action can be written as:

$$p_{\theta}(v_1^*, \dots, v_m^* | G_i) = p_{\theta}(a_1, b_1, r_1, \theta_1, \phi_1, \dots, a_m, b_m, r_m, \theta_m, \phi_m | G_i)$$

Where m is the number of new atoms to add. Compared to most previous autoregressive models for 3D molecules,^{14,15} our proposed method generates all atoms connected to v^* in a single iteration (Figure 5). This has two major advantages. First, it can save computational resources (since the state encoder is run only once for each step). Secondly, since the positions of neighboring atoms are highly correlated, generating them together can potentially improve the model’s performance.

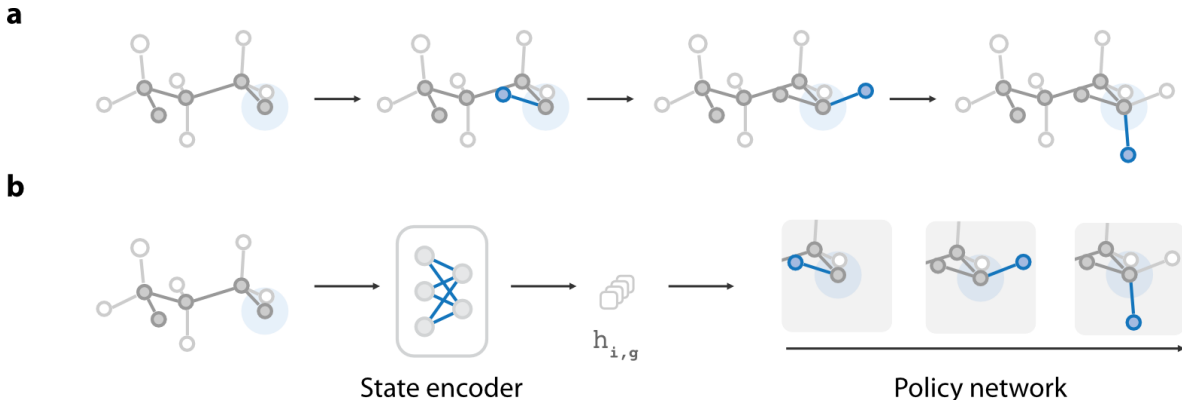


Figure 5: Different from most autoregressive models in 3D molecule generation (a), our proposed method generates all atoms connected to the focused atom as a group (b).

We incorporate several prior knowledge about drug-like molecules. First, most atoms in organic drug-like molecules have a valence less or equal to 4. That is, at most three atoms can be added to a focused atom at one time:

$$p_{\theta}(v_1^*, v_2^*, v_3^* | G_i)$$

When less than three new atoms are added, we add “null” atoms to fill the blanks. This makes the problem simpler since we are now dealing with a fixed number of random variables.

Another prior knowledge we incorporate is that there are only three types of allowed local geometry for most drug-like molecules: sp (linear), sp2 (planar), and sp3 (tetrahedral). We ask the model to first generate the type of the local geometry (h), and then the position of new atoms:

$$p_{\theta}(v_1^*, v_2^*, v_3^* | h, G_i) p_{\theta}(h | G_i)$$

Empirically, we find that this can help the model to better learn the local geometry. Now, we still need to find a way to factorize $p_{\theta}(v_1^*, v_2^*, v_3^* | h, G_i)$, which contains $(2 + 3) * 3 = 15$ random variables. A natural choice is to factorize it into an autoregressive model:

$$p(v_1^*, v_2^*, v_3^*) = p(v_3^* | v_1^*, v_2^*) p(v_2^* | v_1^*) p(v_1^*)$$

$$p(v_i^* | \cdot) = p(\phi_i | a_i, b_i, r_i, \theta_i, \cdot) p(\theta_i | a_i, b_i, r_i, \cdot) p(r_i | a_i, b_i, \cdot) p(a_i, b_i, \cdot)$$

The conditions G_i and h are omitted for simplicity. $p_{\theta}(a_i, b_i | \cdot)$ is a categorical distribution of atom and bond types. We apply prior knowledge about the allowed valence for the focused atom to create a mask for $p_{\theta}(a_i, b_i | \cdot)$ at each step so that it will not violate the valence constraint. $p_{\theta}(r_i | \cdot)$, $p_{\theta}(\theta_i | \cdot)$, $p_{\theta}(\phi_i | \cdot)$ are mixtures of truncated Gaussian distributions. The number of mixture is set to be 15, 10 and 5 for v_1^* , v_2^* , v_3^* respectively. The range of r_i and θ_i are set to $[0.5, 2.5]$ and $[0, \pi]$. The parameters of those distribution are calculated using MADE (masked autoencoder for distribution estimation²⁹), which is an efficient architecture for autoregressive models based on masked linear layers. The architecture for MADE is

demonstrated in Figure 6.

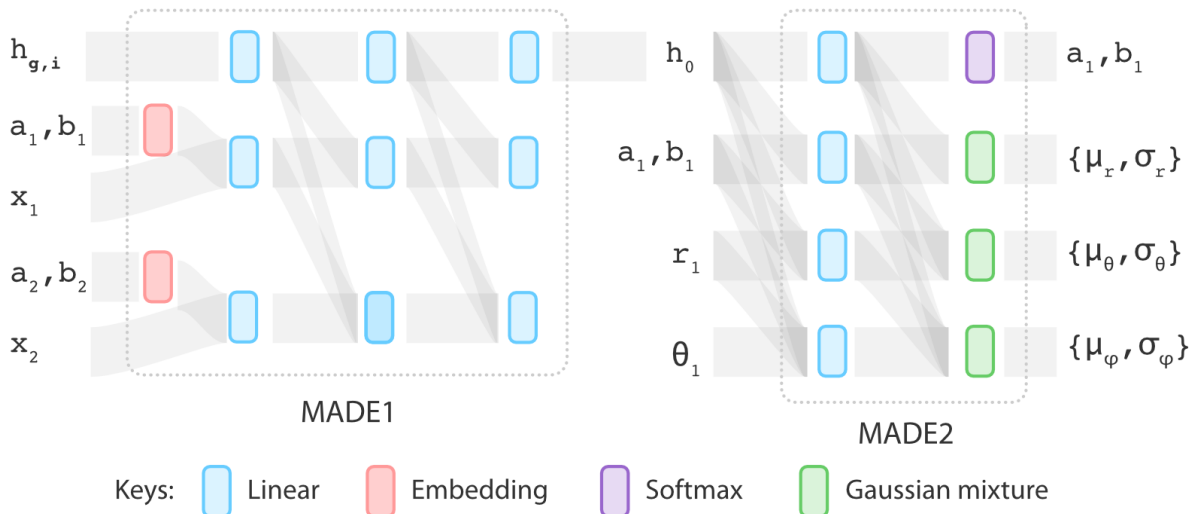


Figure 6: The architecture of MADE blocks. Output sizes of linear layers in the MADE1 block are 128, output sizes of linear layers in the MADE2 block (except that used in the Gaussian mixture layer) are 64. The embedding table used here is the same as that used in the state encoder. The activation function used for outputting standard deviation of r , θ and ϕ is softplus.

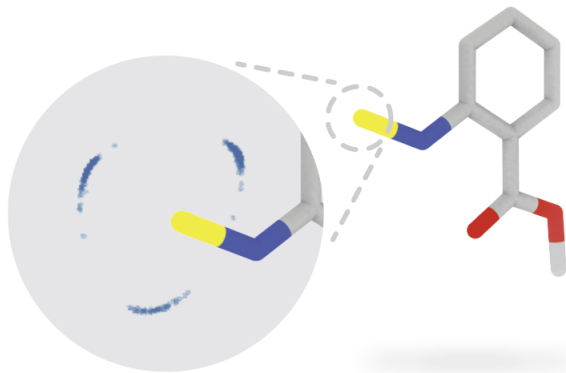


Figure 7: The problem of low dimensionality. This figure shows the new atoms sampled from the model mostly reside inside a 1D ring above the focused atom.

In practice, the target distribution of atom position usually resides in a low dimensional submanifold of \mathbb{R}^3 (Figure 7), and using MADE to directly fit those distributions will not work well. We adopt the method from a previous work³⁰ and adds a small error to the target distribution so that it can be fitted more robustly by MADE. We call this modified model

SoftMADE. Different from the original paper, which samples the noise level from a uniform distribution: $c \sim u[a, b]$, we sample the noise level in two steps:

$$c_0 \sim u[0, 1]$$

$$c = c_{\max} c_0^\alpha$$

Where c_{\max} is the maximum level of noise, and $\alpha > 1$ is the parameter controlling the shape distribution. Three conditons are tested: (1) ordinary MADE; (2) SoftMADE with $c_{\max} = 0.2, \alpha = 3$; (3) SoftMADE with $c_{\max} = 0.4, \alpha = 4$. It is find that bigger c_{\max} combined with higher α (the third conditon) yields better result.

Finally, since the new atoms v_1^*, v_2^*, v_3^* can be generated in any order, we use the following corrected likelihood during training:

$$p(\{v_1^*, v_2^*, v_3^*\}) = 1/3! \sum_{\sigma} p(v_{\sigma_1}^*, v_{\sigma_2}^*, v_{\sigma_3}^*)$$

Decision making during the “connect” operation For each possible action in the “connect” operation, we first compute their unnormalized scores as follows:

$$\hat{\mathbf{p}}_v^{\text{connect}} = \text{MLP}_{\text{policy}}^{\text{connect}}(\mathbf{h}_{i,v})$$

$$\hat{p}_v^{\text{skip}} = \text{MLP}_{\text{policy}}^{\text{skip}}(\mathbf{h}_{i,g})$$

Where $\text{MLP}_{\text{policy}}^{\text{connect}}$ and $\text{MLP}_{\text{policy}}^{\text{skip}}$ are fully connected layers. Those scores are then normalized using softmax:

$$[\mathbf{p}_v^{\text{connect}}, p_v^{\text{skip}}] = \text{softmax}([\hat{\mathbf{p}}_v^{\text{connect}}, \hat{p}_v^{\text{skip}}])$$

The values $\mathbf{p}_v^{\text{connect}}[b]$ in vector $\mathbf{p}_v^{\text{connect}}$ represents the probability of connecting the focused atom v' with v using a new bond of type b . The value p_v^{skip} represents the probability of skipping the “connect” operation and proceeds directly to the “append” operation.

Ranking the generated atoms When ranking the generated atoms, we first calculate an unnormalized score for each permutation of the new atoms:

$$\hat{s}_\sigma = \text{MLP}_{\text{policy}}^{\text{rank}}([v_{\sigma_1}^*; v_{\sigma_2}^*; v_{\sigma_3}^*])$$

And then the normalized probability:

$$p(\sigma) = \frac{\exp \hat{s}_\sigma}{\sum_{\sigma'} \exp \hat{s}_{\sigma'}}$$

The ranking is then sampled from $p(\sigma)$.

2.7 Data collection and preprocessing

We construct a drug-like subset of ChEMBL¹⁸ for the training and evaluation of the model. The topological data of all molecules are downloaded from ChEMBL (version 27) and is then filtered using a series of criteria:

- Molecules with atom type outside the set {C, H, O, N, P, S, F, Cl, Br, I} as well as those that do not contain carbon atoms are removed;
- Molecules with the number of heavy atoms outside the range [10, 35] are removed;
- Molecules with a QED³¹ value less than 0.5 are removed;
- Molecules with ring sizes larger than 7 are removed. Rings in the molecule are extracted using RDKit;
- Molecules containing a ring assemble with the number of SSSR(smallest set of smallest rings) greater than 4 are removed.

After filtering the topological structure, 3D structures are generated for each molecule using RDKit. The initial 3D embeddings of molecules are first created using distance geometry and then optimized using the MMFF94s forcefield. After those processings, we obtain a dataset with 1 million small molecules with 3D structure. The dataset is randomly split into the training set (4/6), validation set (1/6), and test set (1/6). The validation set is used during the manual hyperparameter tuning.

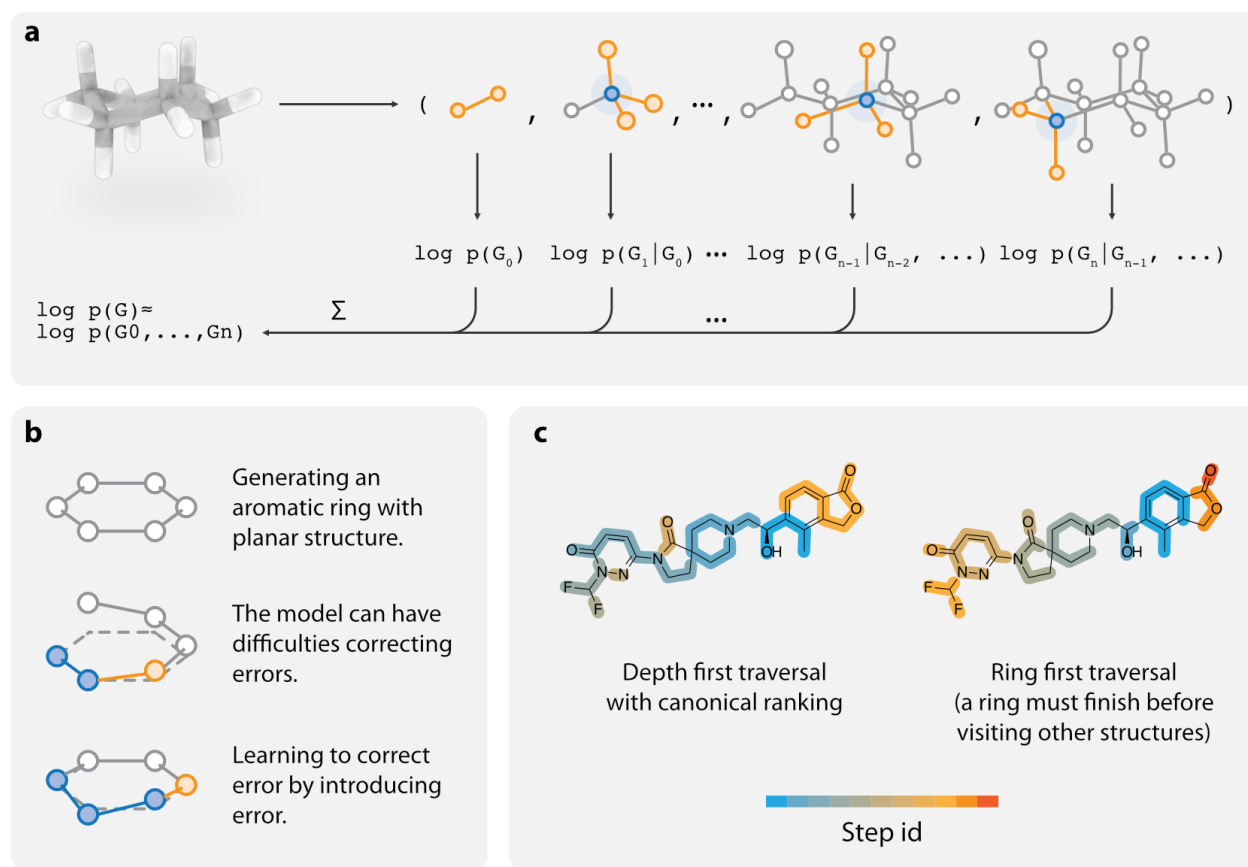


Figure 8: Data preprocessing and tricks used to improve model performance. **a.** For each data in the training set, we create an “expert trajectory” for generating this molecule, and train the model to imitate this trajectory. **b.** We find that the model may suffer from the problem of distribution mismatch, so random errors are manually added to the training data so that the model can learn to correct them. **c.** The image shows the order each atom is traversed for ordinary (left) and ring first (right) traversal scheme (blue atoms are traversed first, red atoms are traversed last). We treat a ring as a basic generation unit and use ring-first traversal to train the model to close the ring first before generating other structures.

As mentioned in previous sections, the model generates molecules in a step-by-step man-

ner. To train the model, we need to create an “expert trajectory” for generating each molecule G in the dataset (Figure 8a):

$$(G_0, G_1, \dots, G_n), \text{ where } G_1 = \emptyset, G_n = G$$

The model is then trained to imitate this path by maximizing the log-likelihood:

$$\log p_\theta(G) \approx \sum_{i=1}^n \log p_\theta(G_i | G_0, \dots, G_{i-1})$$

We use a method similar to that used previously^{7,10} to generate those “expert trajectories”. Briefly, the atoms in the molecule are first ranked using a canonical ranking algorithm in RDKit, and depth-first traversal is performed to produce a path (G_0, G_1, \dots, G_n) . Although this method works well for 2D generative models, it does not produce good results on our 3D generative model. To improve the performance, we modify the depth-first traversal algorithm to prioritize the closure of rings (see Figure 8c). We find that this method could significantly improve the quality of generated samples.

It is also reported that randomized trajectories help the model to achieve better performance.^{7,32} In this work, we randomize the trajectory by randomizing the starting position of the depth-first traversal. We also include data of the model trained using non-randomized trajectories for comparison.

One of the major issues related to imitation learning is data distribution mismatch. Specifically, the model only sees correct “expert trajectories” during training, and if a mistake happens during generate, the model may not know how to recover from that error, and eventually produce invalid results (see Figure 8b for a simple example). Our solution is to “simulate” those errors by adding Gaussian noise to the input by a certain probability. We use a noise with the standard deviation of 0.1 \AA and experimented with the probability of 0.1 and 0.5. It shows that a 0.5 probability significantly improves the model performance compared with the 0.1 level.

2.8 Model training

The model is implemented using PyTorch.³³ Adam³⁴ is used to optimize the model parameter. Parameters (β_1, β_2) are set to be the default value provided by PyTorch. The learning rate is initialized to be 10^{-3} , and is decreased by 0.01 for a certain amount of step. Several decay frequencies are experimented with: every 50 steps, every 100 steps, or every 200 steps. The batch size for training is set to be 128, and are trained for a total of 10 epochs. This takes around 3 days to finish. Training is performed on a single NVIDIA TITAN Xp graphics card.

2.9 Hyperparameters

As can be seen from previous sections, the model proposed here contains a large number of hyperparameters, including those for model architecture, data generation, and model training. Considering the long training time, comprehensive optimization of hyperparameter is difficult. The hyperparameter selection is further complicated by the fact that there are a variety of metrics that can be used to evaluate the model (see section 2.11). The best performing model on one metric does not necessarily performs the best on the other. In this work, we target 3D MMD as the objective and performs manual hyperparameter tuning to get to the performance level that is acceptable for general usage. The result hyperparameter setting is referred to as the “standard” configuration and is what we suggest to use in future research using this model. We do note that the optimization process is not comprehensive and we expect that better performance can be obtained using more dedicated hyperparameter optimization techniques.

To understand how model performance is affected by a set of hyperparameter of interest, we perturb those parameters from the standard configuration to investigate its effect. The set of hyperparameters that is analyzed are (also summarized in Table 1):

- The depth and width of DenseNet (see section 2.4);

- The parameters for SoftMADE (see section 2.6);
- The noise added to coordinates of the input structure (see section 2.7);
- Whether the “expert trajectories” used for training are randomized (see section 2.7).

Table 1: A summary of different hyperparameter configurations whose performance are reported in this work.

Methods	Randomized trajectory	c	alpha	Input noise	DenseNet architecture	Learning rate decay
Non-random initialization	No	0.4	4	0.5	Basic	100 step
SoftMADE (low noise)	Yes	0.2	3	0.5	Basic	100 step
No SoftMADE	Yes	0	0	0.5	Basic	100 step
Low input noise	Yes	0.4	4	0.1	Basic	100 step
Shallow DenseNet	Yes	0.4	4	0.5	Shallow	100 step
Narrow DenseNet	Yes	0.4	4	0.5	Narrow	100 step
Slow lr decay	Yes	0.4	4	0.5	Basic	200 step
Fast lr decay	Yes	0.4	4	0.5	Basic	50 step
Standard configuration	Yes	0.4	4	0.5	Basic	100 step

2.10 Optimizing the speed of molecule generation

We used several techniques to accelerate the process of molecule generation. First, many CPU side operations in this model cannot be implemented efficiently using native python, and we use Numba,³⁵ a just-in-time compiler for python, to speed up those codes. The performance benefit is significant, and in our case, the speedup can be more than 10 times.

Secondly, we use multiprocessing to hide CPU processing latency from GPU. During molecule generation, we need to move back and forth between GPU and CPU for action sampling and graph processing. When a large number of molecules are being generated at

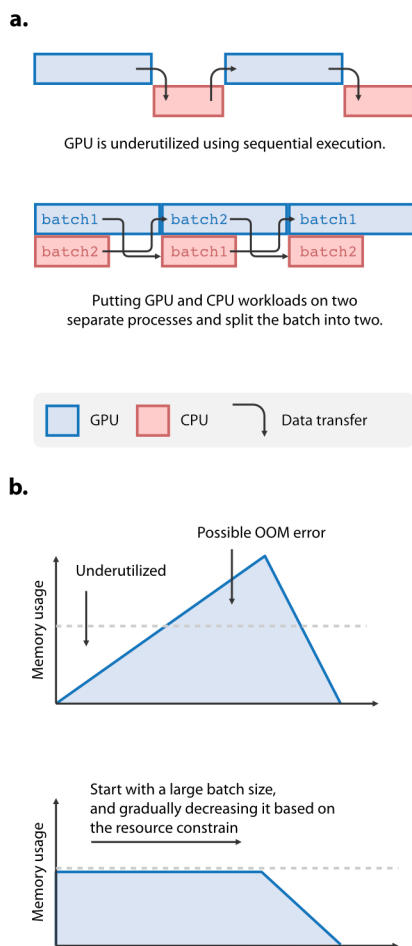


Figure 9: Tricks used to accelerate molecule generation: **a.** CPU and GPU workloads are separated into two different processes and can be executed asynchronously by each working on a different batch of data (batch1 and batch2) at the same time. **b.** Batch size is adjusted dynamically to ensure that GPU is fully utilized and does not exceed the resource constrain.

the same time, the graph processing time in the CPU can be significant. Since GPU operation is blocked by CPU tasks, there will be noticeable performance degradation. Our solution is to place GPU and CPU in different processes and split the molecules being generated into two batches. During CPU processing, GPU can work on the other batch of molecule, thereby increasing the GPU utilization (Figure 9a).

Thirdly, we develop a method to adaptively balancing the number of molecules generated at each time. During molecule generation, as more nodes are added to the molecule, the computational cost for the neural network to process the intermediate structure will be

gradually growing. This will cause a significant performance degradation. At the beginning of generation, the computation burden is low, and GPU is largely underutilized. When approaching the end of the generation, the computation cost is significantly higher, and can cause out of memory (OOM) error (Figure 9b). We created a scheduling method to dynamically adjust the batch size of the generation task based on the maximum capacity of the GPU. Empirically this has resulted in significant speed improvement for our model.

After performing those operations, we can achieve a generation speed of 0.008 seconds per molecule in a NVIDIA TITAN Xp card. Note that this speed is slower than SMILES-based samplers, largely because of the complexity of the generative workflow and the network architecture. But we also note that there are still spaces where the performance can be further improved, like performing quantization or pruning, which will be explored in the future.

2.11 Evaluation

Several benchmarks have been developed for evaluating 2D generative models, such as MOSES³⁶ and GaucaMol,³⁷ but this type of work is still missing for 3D models. Here, we assemble a set of evaluation metrics for assessing the performance of 3D generative models. Emphasis is placed on measuring the quality of molecule conformations, by investigating various 3D molecular features. All the following metrics are calculated using 50,000 generated molecules.

Output validity and uniqueness

The two metrics measure the percentage of output molecules that are chemically valid and structurally unique. The validity is measured by calculating the percentage of generated molecules that pass the RDKit sanitization check (%valid). Although this metric measures the quality of topological structure, we find that in practice it is also a good proxy for the quality of 3D structures. This is because that many serious 3D errors occurring during the generation will eventually lead to invalid topological structures. The uniqueness is measured

by calculating the percentage of unique structures among outputs (%uniq). This can be used to detect whether the model has been overtrained or has collapsed to a single mode.

Distribution of molecular properties

Investigating the distribution of molecular properties is a good way to intuitively assess the quality of generated samples. The mean and standard deviation of each property is reported, as well as the visualization using kernel density estimation. The properties investigated include regular topological features (molecular weight, LogP, the number of hydrogen donors and acceptors, the number of rotatable bonds, QED) as well the following 3D features:

- Normalized PMI ratios (NPRs):³⁸ This is a shape descriptor composed of two components ($NPR1, NPR2$) = $(I_1/I_3, I_2/I_3)$, where I_1, I_2, I_3 are principal moments of inertia sorted by ascending magnitude. The point $(1, 1)$, $(0.5, 0.5)$, $(0, 1)$ corresponds to the archetypes of sphere, disk and rod, giving this descriptor high interpretability. NPRs are calculated using the implementation in RDKit.
- Solvent accessible surface areas (SASA): SASA is an important molecular descriptor measuring the contact area between the molecule and the solvent. We report the distribution of polar and total SASA calculated using the package FreeSASA.³⁹

Maximum mean discrepancy

We use maximum mean discrepancy (MMD) to give a quantitative measurement of the difference between the distribution of generated and real samples. Given a kernel function $\kappa(\cdot, \cdot)$, the MMD between two distributions can be estimated as :

$$MMD = \frac{1}{N(N-1)} \sum_{i=1}^N \sum_{j=1, j \neq i}^N \kappa(x_i, x_j) + \frac{1}{M(M-1)} \sum_{i=1}^M \sum_{j=1, j \neq i}^M \kappa(y_i, y_j) - \frac{2}{MN} \sum_{i=1}^N \sum_{j=1}^M \kappa(x_i, y_j)$$

Where $\{x_i\}_{i=1}^N$ are sampled from the real distribution and $\{y_i\}_{i=1}^M$ sampled from the generative model. This method has been previously used to assess the performance of 2D

molecular generative models,¹⁰ and can be easily applied to 3D models by changing κ to measure 3D molecular similarity.

In this work, we use two types of kernel function to calculate MMD: (1) the Tanimoto similarity of 2D Morgan fingerprint (1024 bit, radius of 2) and (2) the Manhattan distance of USRCAT fingerprint.⁴⁰ The two MMD measures the topological and 3D discrepancy between generated and real samples. Note that for the 3D kernel function, a more accurate choice might be using the shape-based alignment method.⁴¹ But since the computational complexity of MMD calculation is $O(\max(M, N)^2)$, and shape alignment involves optimization for each molecule pair, this will not be feasible for our task. USRCAT is an alignment-free method with precalculated fingerprint and is more suitable for MMD calculation.

The calculation of MMD is parallelized in GPU using Cupy.⁴² For topological fingerprint, we store the 1024 bit fingerprint into 32 uint32 integers and utilize bitwise operations to speed up the calculation of Tanimoto coefficient.

Precision and recall

Although MMD can reliably quantify the discrepancy between distributions, its value is difficult to interpret. Ideally, we want the information about:

- What percentage of generated samples are realistic;
- What percentage of real data distribution can be covered by the generative model;

We call the two metrics precision and recall for the generative model. Precision can be used to measure the sample quality, and recall can be used to assess mode coverage. Since they are both percentage values, they are more interpretable than MMD.

The definition of the two metrics follows the previous work.⁴³ First of all, we define the space covered by a probability distribution from its samples $X = \{x_i\}_{i=1}^N$ as:

$$\Phi(X) = \{x | \exists x_i \in X \text{ s.t. } d(x - x_i) \leq d(N_k(x_i, X) - x_i)\}$$

Where $N_k(x_i, X)$ denotes the k -th nearest neighbor of x_i in the dataset X , and $d(\cdot, \cdot)$ measures the distance between two data point. Given the real data $X = \{x_i\}_{i=1}^N$ and generated data $Y = \{y_i\}_{i=1}^M$, precision and recall are defined as:

$$P = \frac{|Y \cap \Phi(X)|}{|Y|}$$

$$R = \frac{|X \cap \Phi(Y)|}{|X|}$$

Similar to MMD, a 2D and 3D version of precision and recall can be calculated using Morgan fingerprint and USRCAT. The value of k is set to be 3.

Validity of local geometries

We check the correctness of local 3D structures in generated molecules by examining the distributions of bond lengths and bond angles. More specifically, we group the bond lengths and angles by its environment key, calculate the mean and standard deviation within each group, and compare them between generated and test set molecules. The environment key for the bond length contains the bond type and the type of its two adjacent atoms: (a_u, a_v, b_{uv}) , while that for a bond angle contains the type and hybridization state of the central atom: (h_u, a_u) . Groups containing less than 1000 data points are removed from the evaluation.

We also check the distribution of torsion angles in generated and test set molecules. Quads of atoms a-b-c-d are matched using the SMARTS pattern provided in the previous work⁴⁴ and torsion angles are calculated from the matched coordinates. Patterns that give less than 1000 matches are discarded. MMD values of the torsion distribution in each pattern are computed.

The about evaluation aims at giving a qualitative look about the quality of local geomerty, and the comparison is only performed on the model trained with standard configuration. We use RMSD (Root Mean Standard Deviation) for a more quantitative evaluation, as described below.

RMSD

For each generated molecule, we optimize the conformation using MMFF94s force field and calculate the RMSD of heavy atoms between the original and optimized structure.

To give a context on how the model performs in this metric, we perform the same calculation on the ETKDG method,⁴⁴ which is a conformation generation method for small molecules that aims to provide a faster alternative for forcefield-based minimization. For each molecule in the test set, we generate an initial conformation using ETKDG, optimize it using MMFF94s, and calculate the RMSD for conformation before and after optimization. The average RMSD is then compared with that of the generative model.

Note however that since ETKDG and deep generative model is developed to solve two completely different problems, the comparison of RMSD can not tell which method is better or worse. Nonetheless, this comparison should give us an idea about the overall level of quality of the generated conformations.

2.12 Combining L-Net with MCTS for structure-based molecule design

The model proposed in this work can be conveniently combined with other techniques such as reinforcement learning to achieve molecular design based on a given objective. As a proof of concept, we combine L-Net with Monte Carlo tree search (MCTS) and test its ability in the problem of structure-based molecule design. Previous works have combined MCTS with 2D generative models in the object-directed design of molecules,⁴⁵ but to our knowledge, the combination of MCTS with 3D generative models has not yet been reported.

Technically, we use L-Net as the rollout policy for MCTS, and Maximum Entropy for Tree Search (MENTS)⁴⁶ for tree policy. We periodically perform an “exploit” step that samples directly from the distribution defined by the Q-values. For each sample, local optimization is performed using smina,⁴⁷ and the resulted (minus) affinity score is treated as the reward function. Note that the optimization is only performed locally not globally, so the evaluation process can be done extremely fast. Water molecules are striped from the structure before

scoring using smina. To better utilize the computational power of GPU, leaf-level and tree-level parallelization is introduced to MCTS, similar to that done by Chaslot et al.⁴⁸

The case target that we use to test the model is the Tyrosine-protein kinase ABL1, which is related to chronic myelogenous leukemia (CML). Instead of the frequently targeted ATP-site, here we focus on the allosteric myristate binding site due to its potential advantages in selectivity. However, using binding affinity scores from smina to guide the design of allosteric inhibitors might be problematic. Indeed, previous works have reported several binders of the ABL1 allosteric site with no inhibition activity.⁴⁹ Instead of trying to generate the entire structure using L-Net, we use the *CClF₂O-* group in asciminib (a known active molecule currently under clinical trial, see Figure 20b) as seed structure. Previous reports have shown that this functional group is essential for the inhibition activity of asciminib.⁴⁹ Based on this seed structure, we then use the L-Net with MCTS to generate and optimize the rest of the structure for higher binding affinity.

3 Results and Discussion

3.1 Generated samples, validity and uniqueness

Several randomly generated samples are shown in Figure 10a, with topological and 3D structures (rendered using ChimeraX⁵⁰). Visual inspection shows that those molecules have correct local geometry. For example, sp3 and sp2 hybridized atoms correctly adopt tetrahedral and planar geometry, and aromatic systems correctly form planar structures.

Table 2: The performance of LNet, measured in terms of %valid and %uniq, with different hyperparameters. The star indicates the best performing hyperparameter selection.

Method	%Valid	%Uniq
Non-random initialization	93.4%	98.7%
SoftMADE (low noise)	92.5%	99.0%

Method	%Valid	%Uniq
No SoftMADE	89.8%	89.7%
Low input noise	88.2%	97.4%
Shallow DenseNet	90.5%	98.9%
Narrow DenseNet	90.7%	98.6%
Slow decay	94.3% (*)	98.2%
Fast decay	87.2%	99.0%
Standard configuration	93.5%	99.1% (*)

Table 2 demonstrates the ability of LNet to generate valid (measured by %valid) and unique (measured by %uniq) molecules. Our model can achieve as high as 94.3% of output validity. For %uniq, the reported values are generally approaching 100%, indicating no overtraining or mode collapse. Note in the result that using SoftMADE (row 9 v.s. row 2 and row 3) significantly improve the model’s performance in terms of %valid, indicating that naive MADE indeed suffers from the problem of low dimensional manifold (discussed in Section 2.6) in our task. The addition of input error (row 9 v.s. 4) also helps to improve the performance of %valid, likely due to the reason discussed in Section 2.7. Note however that randomized trajectory (row 9 v.s. row 1) does not significantly improve model performance. This might be because we only randomized the selection of the first atom. We find that using techniques such as temperature sampling can further improve the %valid value. However, we find that this method would significantly reduce other performance metrics such as MMD, and is therefore not adopted.

Other works in the 3D generative model have reported much lower %valid values. Gebauer et al. have reported a 77.07% result on %valid¹⁴ using QM9, which is structurally much simpler than the dataset we use. Ragoza et al. reported a closer 90% result on %valid,¹⁷ using molecules from the MolPort dataset, but their method is not end-to-end and requires separate atom placement and bond order assignment algorithms. We also note that the %valid

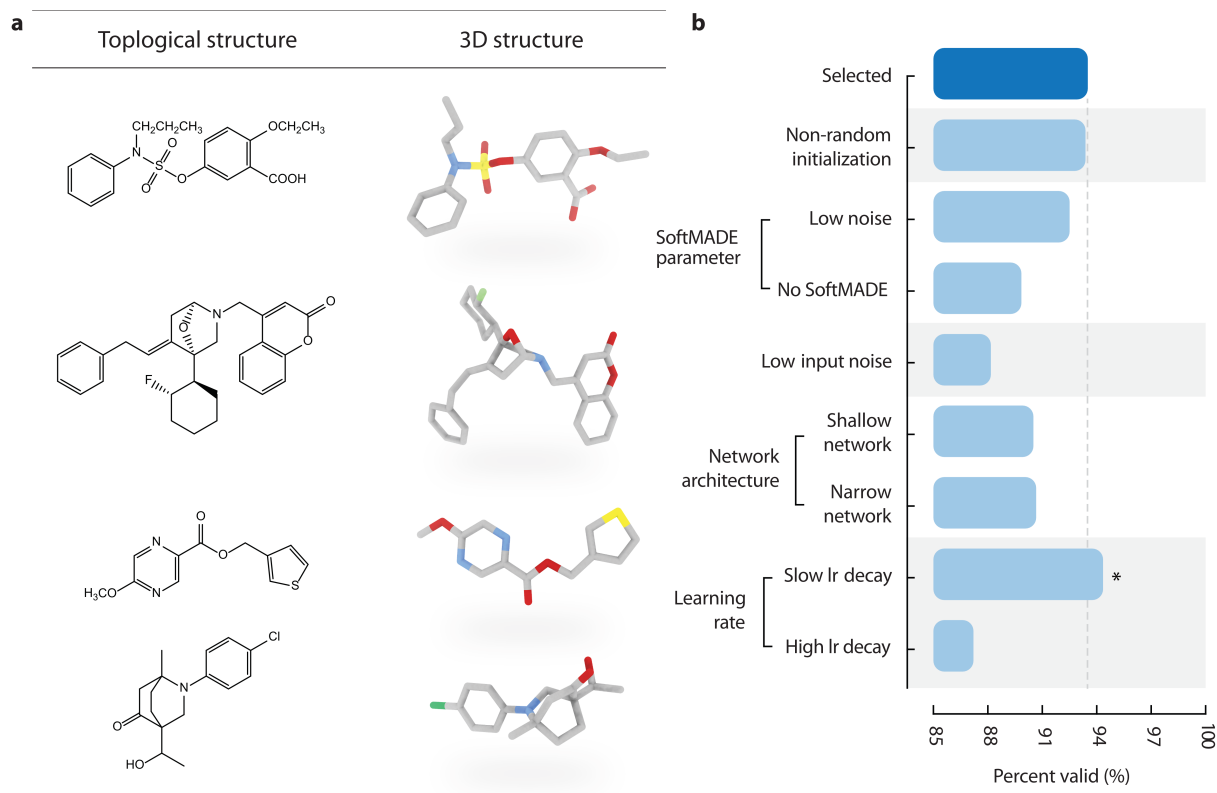


Figure 10: **a**. Several randomly generated samples from LNet; **b**. The percentage of output molecules with valid chemical structures, depending on the different selection of hyperparameters. The star indicates the best performing hyperparameter selection.

result for our model is lower than most 2D generative models, even simple SMILES-based methods. This phenomenon is also reported in the result of G-SchNet.¹⁴ The major reason is that for our model, not only topological errors will contribute to invalid molecules, but also 3D ones. In fact, most 3D errors will eventually be converted to topological errors in our model. This means that 3D generative tasks for molecule exhibits higher difficulty compared with 2D tasks.

3.2 Distribution of molecular properties

Table 3: Distribution of 2D molecular properties among generated molecules using different hyperparameters.

	MW		LogP		HBA		HBD		ROTB		QED	
Methods	mean	std.	mean	std.	mean	std.	mean	std.	mean	std.	mean	std.
Non-random initialization	328.5	86.8	2.89	1.45	4.00	1.67	1.25	0.95	4.26	2.25	0.683	0.148

	MW	LogP	HBA	HBD	ROTB	QED						
SoftMADE (low noise)	332.0	87.6	2.87	1.47	4.06	1.71	1.29	0.99	4.18	2.18	0.675	0.152
No SoftMADE	329.0	94.3	2.86	1.55	4.07	1.80	1.20	0.98	4.20	2.28	0.664	0.156
Low input noise	356.4	119.1	2.66	1.68	4.72	2.11	1.47	1.10	4.76	2.79	0.588	0.182
Shallow DenseNet	338.9	95.3	2.84	1.55	4.21	1.78	1.31	1.01	4.29	2.30	0.662	0.158
Narrow DenseNet	329.0	93.3	2.74	1.52	4.17	1.79	1.20	0.98	4.22	2.26	0.669	0.154
Slow decay	332.8	90.4	2.78	1.48	4.21	1.75	1.35	1.02	4.51	2.35	0.664	0.152
Fast decay	339.5	94.3	2.88	1.57	4.17	1.78	1.26	1.01	4.54	2.40	0.655	0.162
Standard configuration	338.0	91.7	2.91	1.55	4.12	1.75	1.26	0.99	4.40	2.28	0.665	0.156
Validation	345.0	69.7	3.05	1.30	4.13	1.55	1.19	0.91	4.30	2.04	0.700	0.117
Test	344.8	69.7	3.05	1.29	4.13	1.56	1.20	0.90	4.30	2.04	0.701	0.116

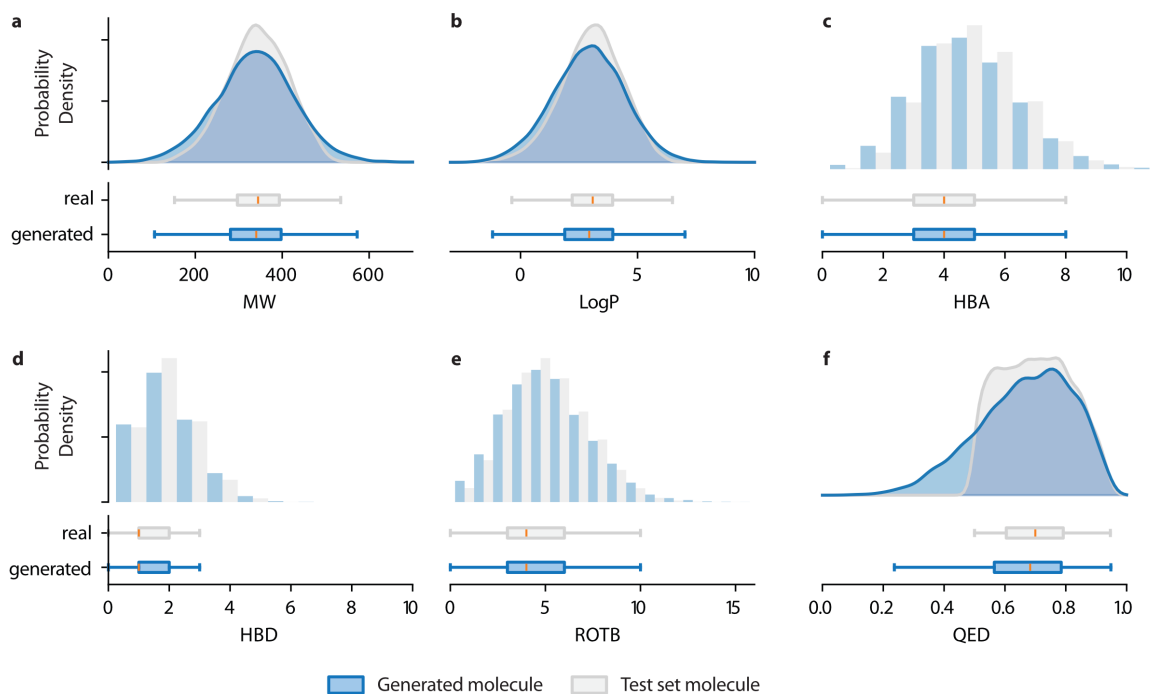


Figure 11: The distribution of 2D molecular properties of generated molecules and test set molecules. **a.** Molecular weight (MW). **b.** LogP. **c.** The number of hydrogen bond acceptors (HBA). **d.** The number of hydrogen bond donors (HBD). **e.** The number of rotatable bonds (ROTB). **f.** Druglikeness (QED). Generated molecules are shown in blue, and test set molecules are shown in grey.

We first investigate the topological properties of generated samples. Table 3 shows the mean and standard deviation of various topological properties among the generated samples and samples in the validation and test set, using different combinations of hyperparameters. Figure 11 give a visualized presentation of the distribution for generated (blue) and test set molecules (grey), either using the probability value from kernel density estimation or

using histogram from continuous properties. Horizontal box plots are also given (below the histograms).

The first thing that we may notice is that the property of generated molecule tends to be more spread than that in the test set. This can be demonstrated by the standard deviation of each property shown in Table 3. This may be an indication that the model is prioritizing mode coverage over precision, which is also supported by the result of precision and recall values (see Section 3.4). The mean values of each property match quite well, for molecule weight, the difference is less than 10(row 9 v.s. row 10 and 11). It is also noticed that a large discrepancy is found between the generated and real QED distributions (Figure 11 f). This is the result of a hard cutoff value of 0.5 during data selection.

Table 4: Distribution of 3D molecular properties among generated molecules using different hyperparameters.

	Total SASA		Polar SASA		NPR1		NPR2	
Methods	mean	std.	mean	std.	mean	std.	mean	std.
Non-random initialization	514.9	100.1	126.2	57.6	0.252	0.130	0.859	0.092
SoftMADE (low noise)	518.6	100.8	129.4	58.3	0.252	0.130	0.859	0.093
No SoftMADE	514.6	107.5	128.1	60.3	0.261	0.131	0.854	0.094
Low input noise	540.3	135.9	148.8	66.9	0.278	0.134	0.848	0.095
Shallow DenseNet	524.7	107.6	133.3	59.5	0.263	0.134	0.856	0.093
Narrow DenseNet	514.3	106.5	128.8	59.7	0.265	0.132	0.854	0.094
Slow decay	522.2	104.5	132.1	58.7	0.256	0.132	0.858	0.093
Fast decay	525.3	106.9	129.2	59.6	0.271	0.136	0.856	0.093
Standard configuration	565.9	107.9	129.0	60.2	0.263	0.133	0.857	0.093
Validation	579.5	88.5	129.5	55.9	0.232	0.125	0.869	0.093
Test	537.8	84.0	128.6	53.5	0.232	0.124	0.869	0.093

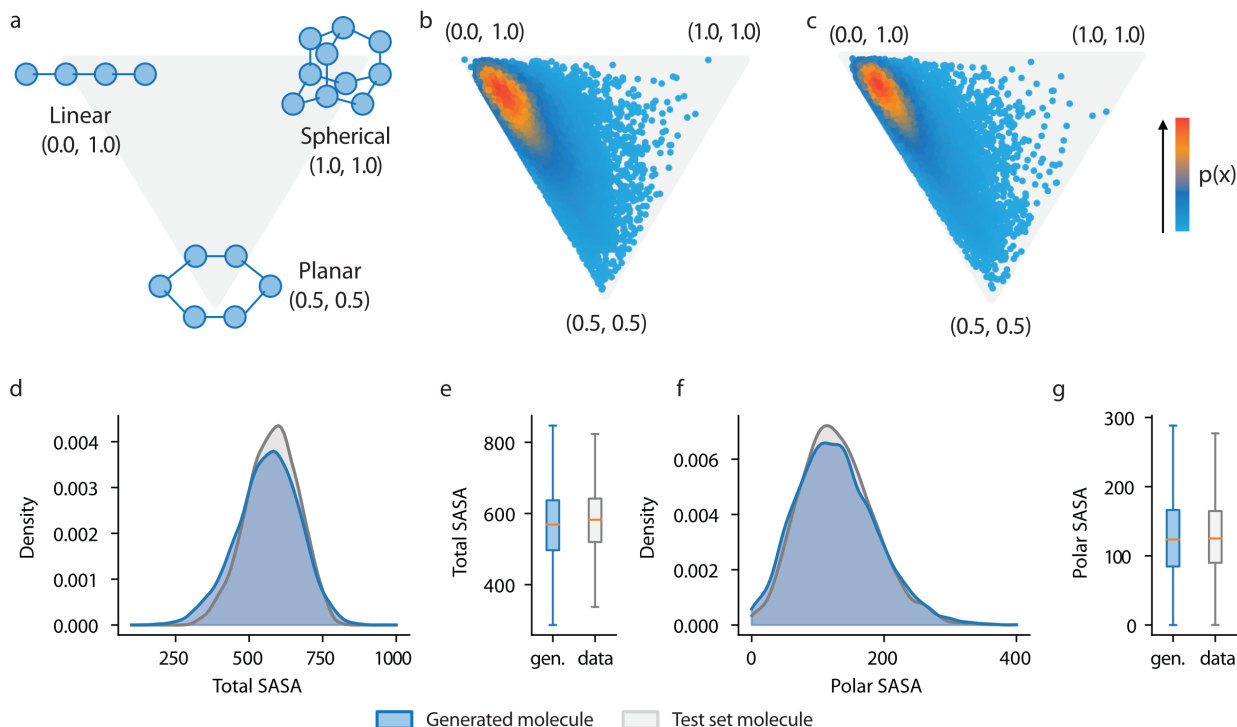


Figure 12: The distribution of 3D molecular properties. **a**. Interpreting the NPR shape descriptors. **b-c**. Comparing the distribution of NRPs between generated (**b**) and test set (**c**) molecules. **d-g**. Comparison of Total SASA and Polar SASA between generated and test set molecules (**d,f**: Kernel density estimation; **e, g**: Box plot; Blue: generated molecules; Grey: test set molecules).

Table 4 and Figure 12 shows the distribution of 3D properties among generated, validation set and test set molecules. Total and polar SASA measures the surface accessible surface area of molecules, and NPR1 and NPR2 measures the overall shape of the molecule (linear, planar, or spherical, see Figure 12a). Similar to that discovered in the distribution of 2D properties, generated samples generally exhibit a wider probability distribution of 3D properties. This discrepancy is not so evident when inspecting the visualized data in Figure 12. For both generated and test set molecules, the shape distribution tends to gather around the “linear” corner of the triangle, while slightly tilted towards the “planar” corner.

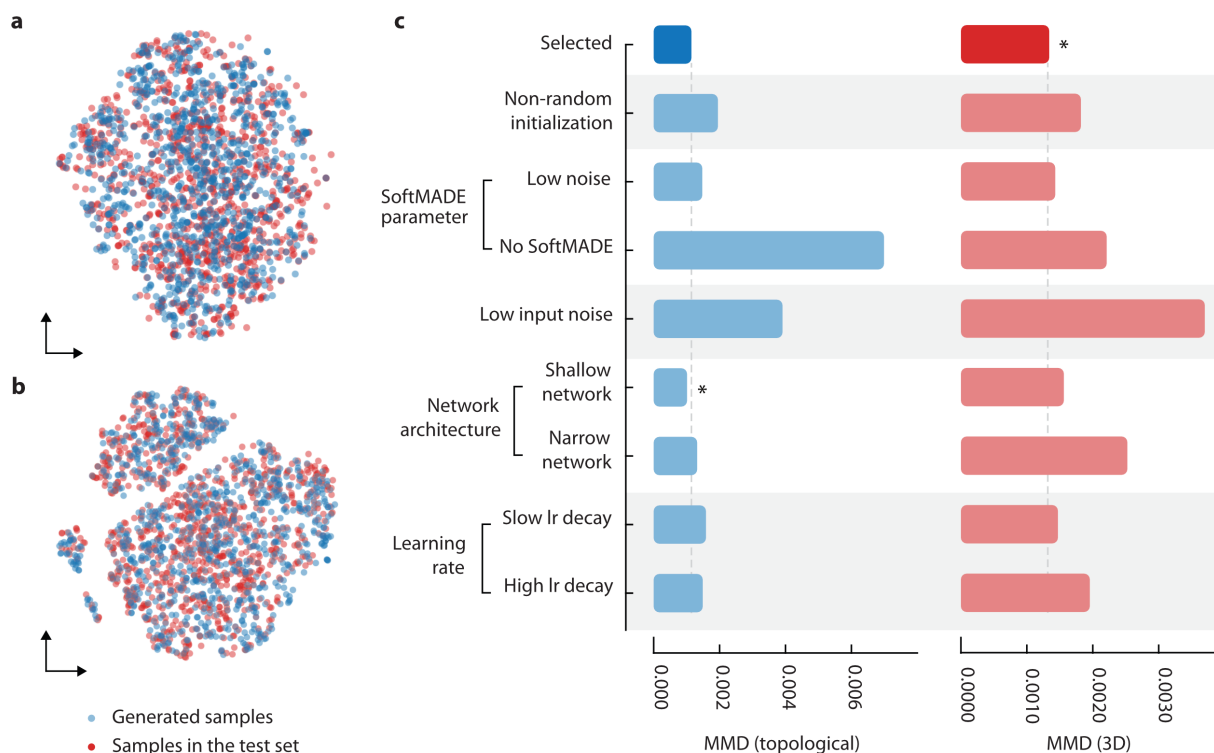


Figure 13: **a-b.** A t-SNE visualization of the distribution of Morgan (**a**) and USRCAT (**b**) fingerprint in two dimension space (Blue: generated samples; Red: samples in the test set). **c.** The Topological and 3D MMD result in the form of bar plot. A star indicates the best performing combination of parameters in that metric.

3.3 MMD and diversity

After a qualitative inspection of sample quality using %valid and property distribution, we move to a more quantitative approach at measuring the discrepancy between the distribution of generated and real molecules. Topological and 3D MMD values are calculated from Morgan fingerprints and USRCAT respectively. A visualization of the distribution of those fingerprint is demonstrated in Figure 13 **a, b**. The high dimensional representation of molecule in fingerprint is embedded into two-dimensional space using TSNE⁵¹ (implemented in scikit-learn⁵²). It is found that generated samples and samples in the test set are evenly mixed in the two-dimensional space, therefore indicating that there is not significant mismatch between the generated and test set samples.

The result of Topological and 3D MMD values are demonstrated in Figure 13 **c** and

Table 5. We start by inspecting the result of topological MMD. It is quickly discovered that SoftMADE and input noise significantly improve the result of topological MMD. This may be contributed by the fact that SoftMADE and input noise reduce errors during the generation. Errors may happen more frequently on topologically complexed molecules, thereby causing the discrepancy between 2D structure distribution. Other hyperparameters do not have a significant effect on topological MMD. Interestingly, having shallow neural network architecture even slightly improves the MMD value. However, using a shallow network does have a significantly negative impact on other metrics (such as %valid), so it should not be the architecture of choice for this task. For 3D MMD, the trend is similar for different hyperparameter selections.

Table 5: The result of topological and 3D MMD, sample diversity, precision and recall for each combination of hyperparameters.

Methods	3D				Topological			
	MMD	Diversity	Precision	Recall	MMD	Diversity	Precision	Recall
Non-random initialization	0.00182	0.154	83.6% (*)	87.8%	0.00195	0.160 (*)	51.4% (*)	71.8%
SoftMADE (low noise)	0.00143	0.155 (*)	83.1%	88.2%	0.00148	0.158	46.6%	74.8%
No SoftMADE	0.00221	0.131	81.8%	88.3%	0.00699	0.158	39.2%	76.8%
Low input noise	0.00370	0.143	76.0%	88.6%	0.00391	0.148	28.8%	84.1% (*)
Shallow DenseNet	0.00156	0.151	81.5%	88.2%	0.00101 (*)	0.156	41.8%	76.8%
Narrow DenseNet	0.00253	0.148	81.7%	88.4%	0.00132	0.157	41.6%	76.6%
Slow decay	0.00147	0.151	81.9%	88.3%	0.00159	0.155	44.9%	76.5%
Fast decay	0.00196	0.150	80.9%	88.6% (*)	0.00149	0.156	38.7%	79.0%
Standard configuration	0.00134 (*)	0.152	81.9%	88.3%	0.00115	0.157	43.1%	78.0%
Validation	-	0.157	-	-	-	0.157	-	-
Test	-	0.157	-	-	-	0.157	-	-

3.4 Precision and recall

The disadvantage of MMD is that its absolute value is not interpretable. Comparatively, precision and recall can provide more insight into how the model performs. The way we calculate those two values is shown in Figure 14. Essentially, precision indicates how many generated records are realistic, while recall indicates how many structures in real samples have been covered by the generative model. The result is shown in Table 5.

We start by analyzing the result for topological structure. The standard hyperparameter

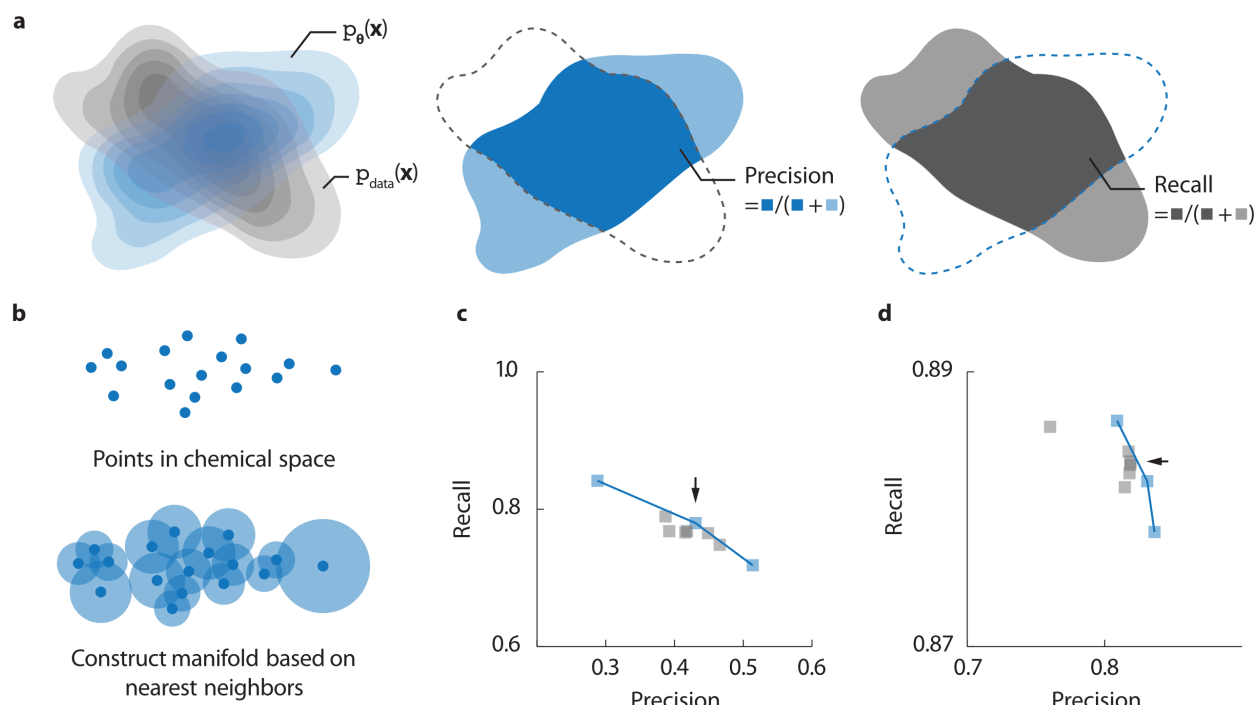


Figure 14: **a.** The method of calculating precision and recall for generative models. Precision is calculated as the percentage of generated samples covered by real samples, while recall is calculated as the percentage of real samples covered by generated samples. **b.** The space covered by a probability distribution is estimated from its samples, using k-nearest neighbors; **c-d.** The precision and recall values calculated using topological (**c**) and 3D fingerprint (**d**), the blue line indicates the Pareto frontier, the black arrow indicates the location of the model with standard hyperparameter configuration.

configuration achieves values of 43.1% and 78.0% for the precision and recall respectively. It is noted that the recall value is significantly higher than the precision value, meaning that a large portion of the real dataset can be covered by the model, but the model will also generate a high portion of molecules that are not realistic. Comparatively, the precision and recall values for 3D structures are much higher. The model with standard configuration achieves 81.9% and 88.3% precision and recall respectively. This higher value might be explained by the abstract nature of USRCAT fingerprint. In fact, USRCAT does not contain explicit information about detailed molecular structure, but instead focuses on pharmacophore distribution in 3D space. Higher precision and recall, in this case, might indicate that the model can better model those 3D pharmacophore features compared with explicit 2D features.

Precision and recall are two distinct evaluation metrics, and optimizing those metrics involves multi-objective optimization. Figure 14 shows the scatter plot of precision and recall for topological structures and 3D structures respectively. The Pareto frontier is colored in blue. The point representing the standard hyperparameter configuration is indicated using a black arrow. Note that the standard configuration lies in the Pareto frontier in Figure 14 **c**, and is close to the frontier in Figure 14 **d**.

3.5 The validity of local geometries in generated molecules

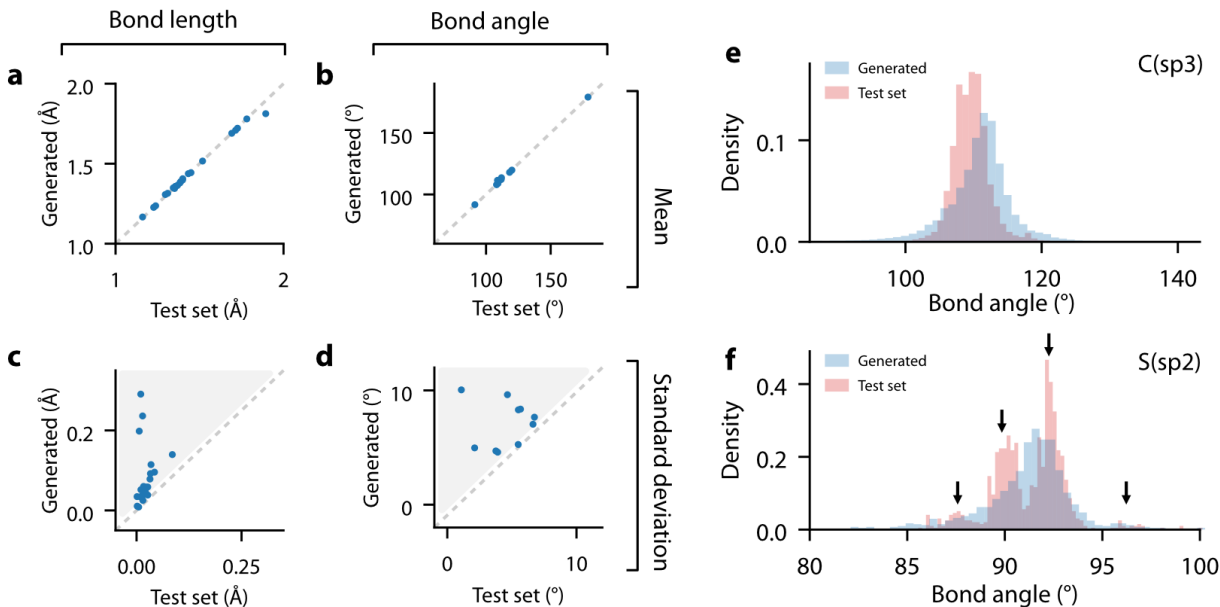


Figure 15: Comparing the distribution of bond lengths and bond angles between generated and test set molecules. **a-b**. Average bond lengths (**a**) and bond angles (**b**) for each environment key in generated (y-axis) and test set (x-axis) molecules. **c-d**. Standard deviation of bond lengths (**c**) and bond angles (**d**) each environment key in generated (y-axis) and test set (x-axis) molecules. **e-f**. The distribution of bond angle in two atomic environments: **e**. sp³ hybridized carbon atom; **f**. sp² hybridized sulfur atom.

The mean and standard deviation for the distribution of bond lengths and bond angles in different environment are shown in Figure 15 **a-d**. The horizontal axis indicates the statistics for test set molecules, while the vertical axis indicates that of the generated molecules.

Figure 15 **a** and **b** shows that the model could learn the average bond lengths and angles

very well, as all points in the scatter plot resides closely to the diagonal line ($y = x$). For standard deviation (Figure 15 **c** and **d**), it is observed that the points in the scatter plot mostly reside above the diagonal line, indicating that the model overestimates the variation in bond lengths and angles. For the standard deviation of bond length, it can be seen that most points lie close to the diagonal line, while a small number of points exhibit large deviations. However, those cases can be easily corrected by manually reducing the standard deviation during generation.

The mismatch is more significant for the standard deviation of bond angles. To better understand the problem, we investigate the distribution of bond angles for two atomic environments (sp³ hybridized carbon atom and sp² hybridized sulfur atom), as shown in Figure 15 **e** and **f**. It is found although there are some deviations in the shape of the distribution (most significantly for sp² hybridized sulfur atom, see the black arrows in Figure 15 **f**), the model still correctly predicts the mean and the range of the distribution. Considering that we have also introduced a mechanism for the model to automatically adapt to minor errors 2.7, this mismatch should not be problematic for the application of the model.

Next, we compare the distribution of torsion angles between generated and test set molecules. The MMD values of the torsion distribution in different environment are shown in Figure 16 **a** (ranking from the lowest MMD to the highest). To make the result more interpretable, we select three environments with the lowest MMDs, three environments with medium MMDs, and three environments with the highest MMDs, and plot the distribution of torsion angles for each case in Figure 16. The result shows good matches between generated (blue) and real (red) molecules in 8 out of 9 cases, which means that the model correctly fits the distribution of torsion angle for most of the time. A notable exception is the last case, where the tendency for cis and trans conformation is essentially reverted in the generated samples.

To summarize, we believe that most of the molecules produced by the model will have valid local geometry. The results do indicate some imperfections in the generated structures,

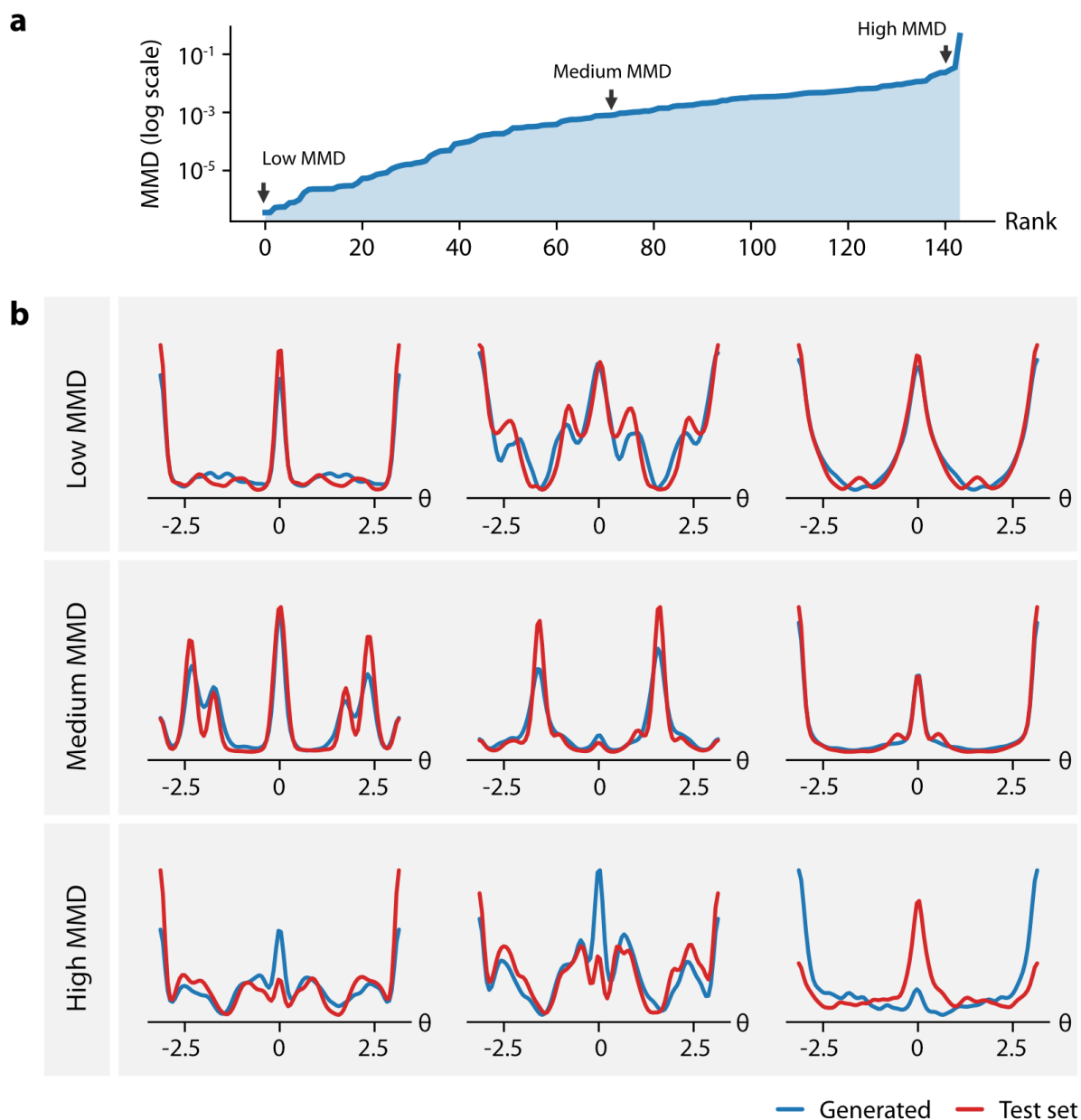


Figure 16: Comparing the distribution of torsion angles between generated and test set molecules. **a.** The MMD values of the torsion distribution for each pattern, ranked from lowest to highest. **b.** Torsion distributions with the highest, medium and lowest MMD values. Blue line indicates the generated samples, and red lines indicates samples in the test set.

but those imperfections are comparatively small and should have a limited impact on the overall conformation of the molecule. Also, if desired, those errors can be easily corrected by including a fast relaxation step using forcefields such as MMFF94s.

3.6 Quality of generated conformers

Table 6: The RMSD values of generated conformers before and after optimization.

Methods	RMSD	
	mean	std.
Non-random initialization	0.613	0.502
SoftMADE (low noise)	0.632	0.508
No SoftMADE	0.715	0.549
Low input noise	0.779	0.597
Shallow DenseNet	0.687	0.533
Narrow DenseNet	0.689	0.522
Slow decay	0.623	0.503
Fast decay	0.735	0.540
Standard configuration	0.663	0.521
Validation	0.838	0.539
Test	0.807	0.524

We evaluate the quality of generated conformations of molecules by calculating the RMSD value between the structure before and after the MMFF94s force field optimization. The average and standard deviation of RMSD are summarized in Table 6 for each hyperparameter choice. Figure 17 shows several randomly generated samples and the aligned 3D structures before and after optimization. It can be seen that although the model can not perfectly generate molecules at the local minima of MMFF94s, the conformation difference before and after the optimization is relatively small. In fact, the best hyperparameter set (disable randomized trajectory) is able to achieve an average RMSD value of 0.613 Å. For other selection of hyperparameters, the value is generally around 0.7 Å. The variance of the RMSD value is rather large. Figure 18 shows the distribution of RMSD among generated

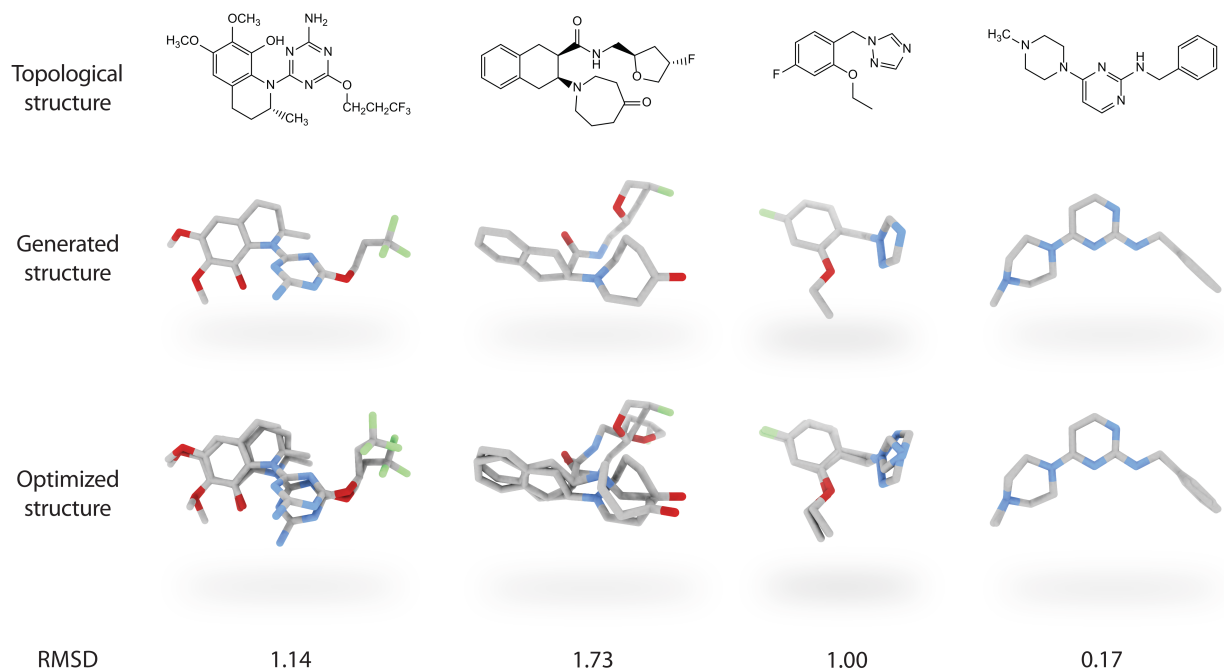


Figure 17: The topological structures, generated conformation, optimized conformation and RMSD value for some generated molecule from the model.

molecules, which concentrates in 0-1 Å but have heavy tailing.

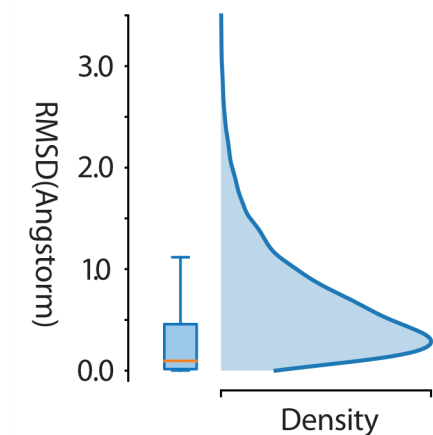


Figure 18: The distribution of RMSD values for generated molecules (from model trained using the standard hyperparameter configuration)

To better interpret the RMSD values, we perform the same calculation using the ETKDG generated conformation of the validation and test set. ETKDG,⁴⁴ which stands for Experimental-Torsion Distance Geometry with “basic knowledge”, is a conformation generation method

combining distance geometry with information about torsion distribution derived from crystallographic data, and is initially developed as a faster alternative to forcefield based optimization. The result shows that the RMSD between the optimized and unoptimized conformation generated using ETKDG is around 0.8 Å (validation set: 0.838 Å, test set: 0.807 Å), which is around 0.2 Å larger than the best-reported RMSD value. The comparison demonstrated that the model-generated conformations might be closer to the local minimums of MMFF94s than that produced by ETKDG. This is an expected outcome since the model is trained directly with data points sampled using MMFF94s, while ETKDG is trained without knowing the forcefield. To summarize, although the model is unable to achieve a perfect result with near-zero RMSD, it should still be able to reach similar or higher performance compared with ETKDG, which is a currently widely used method for 3d conformation generation.

3.7 Structure-based molecule design using L-Net and MCTS

Finally, we combine the L-Net with MCTS to demonstrate its potential in structure-based molecular design problems. The allosteric site of ABL1 is used as a case study. The structure of ABL1 is shown in Figure 20 **a** along with its inhibitor asciminib (PDB ID: 5mo4). The topological structure of asciminib is shown in Figure 20. We start with the seed structure containing the *CClF₂O-* group to ensure the inhibition activity against ABL1 and use MCTS to grow the rest of the structure for high binding affinity (calculated using smina).

We first investigate how fast L-Net and MCTS can generate molecules with a high predicted binding affinity, defined by a predicted binding affinity score < -9.0 . Figure 19 **a** shows how the cumulative number of generated samples with high predicted binding affinity changes with time. Two hyperparameter sets have been tried for MCTS, one with a higher exploration factor (the red line), one with a lower (the blue line). The speed of the model is compared against that of virtual screening (using smina, performed on the ChEMBL dataset). We use 1 CPU core and 1 NVIDIA TITAN Xp to run L-Net with MCTS, and 5

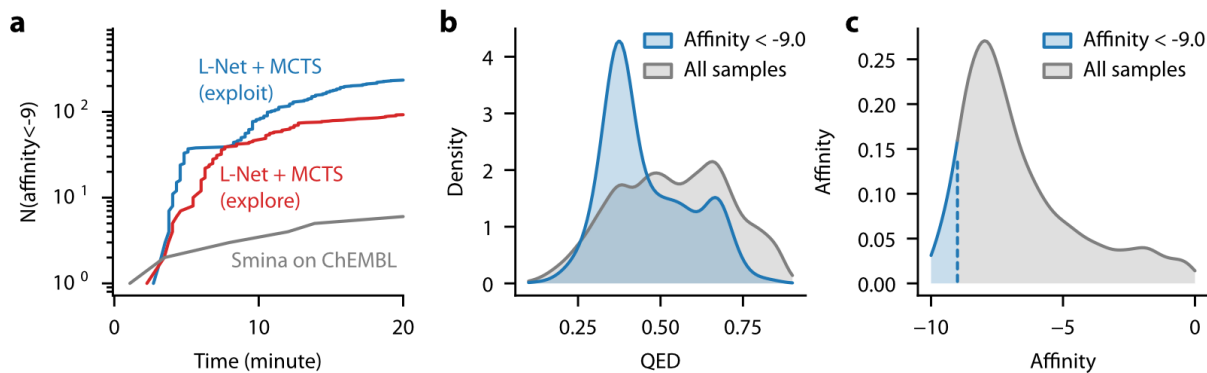


Figure 19: **a.** The speed of model for generating molecules with high predicted affinity, compared with pure virtual screening with smina. **b.** The drug-likeness of all generated samples (grey) and those with high predicted affinity (blue). **c.** The distribution of predicted binding affinity among generated samples. The portion with high affinity value are highlighted as blue.

CPU cores to run virtual screening using smina. All models are run for 20 minutes. The result shows that L-Net combined with MCTS generates molecules with high predicted binding affinity faster than pure virtual screening. The speed is faster for MCTS with a lower exploration factor.

Next, the distribution of drug-likeness (measured with QED) and binding affinity among generated molecules are examined. We will focus on the model with a low exploration factor due to its better performance. Figure 19 **b** shows the distribution of QED among all generated samples (grey) and those with high predicted affinity (blue). Note that the overall drug-likeness is lower compared to unconditionally generated samples (see Figure 11 **f**), and is even lower for those with high predicted affinity. This demonstrates the trade-off the model needs to make between affinity and drug-likeness. Nevertheless, it can be seen that there is still a significant portion of highly drug-like molecules ($\text{QED} > 0.5$) among those with high predicted affinity, providing plenty of candidates for the user to choose from. The distribution of binding affinity is shown in Figure 19 **c**, which concentrates around the affinity value of -7.0. The portion of molecules with high predicted affinity is colored in blue.

A high-quality subset is subsequently obtained from the generated molecules. Only molecules with a predicted affinity < -9.0 will be retained. Those with $\text{QED} < 0.5$ will

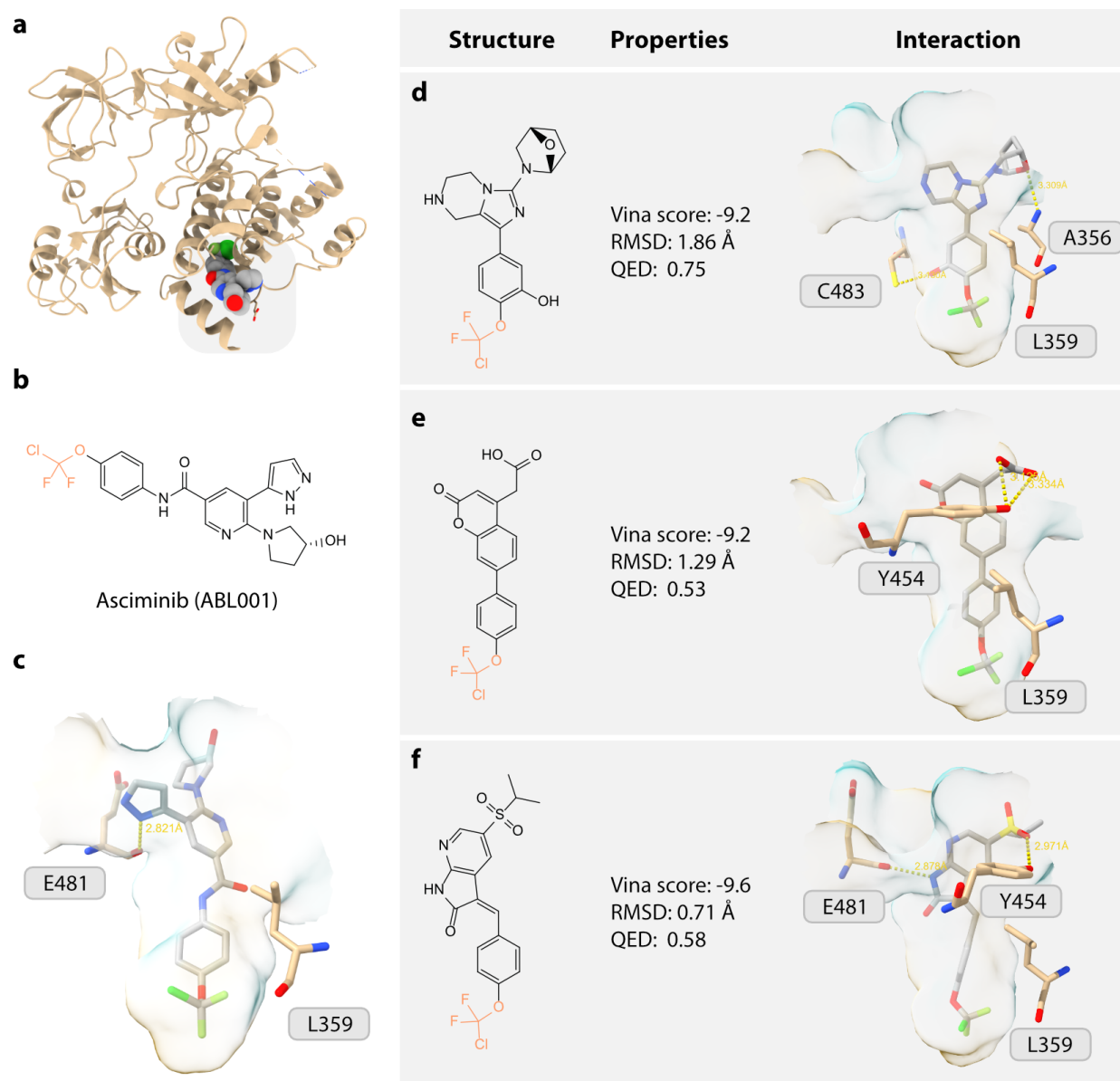


Figure 20: **a.** The structure of asciminib binding to the allosteric pocket in ABL1. **b.** The topological structure of asciminib, with the seed structure highlighted. **c.** A closer look of asciminib inside the binding pocket. **d-f.** The structures of three selected molecules from generated samples and their binding poses predicted by smina.

be filtered out. We also filter out results with $\text{RMSD} > 2.0$ before and after local optimization by smina. The rest of the molecules are manually inspected and three examples are chosen and are shown in Figure 20 **d-f**. We found that most molecules will generate a benzene ring right after the seed structure. This might have resulted from the hydrophobicity of that area in the pocket, as we are able to identify a nearby hydrophobic center

using CavityPlus. In comparison, the amide group in asciminib generally does not occur in the generated structures. It was previously reported that this structure is involved in water-mediated H-bonding interaction to the protein. Therefore, the absence of the amide group might be explained by the lack of water during smina scoring. The “top” portion of the generated structures generally involves hydrogen bonding with the protein. Note that the generated structure in Figure 20 **f** also interacts with E481, similar to asciminib, but from a different direction. The predicted binding affinity is also similar for the two molecules (both have a value of -9.6 after local minimization).

4 Conclusion

In this work, we introduce L-Net, a novel deep generative model for 3D drug-like molecules. Previous works on this direction have either focused on structurally simple molecules with limited drug-likeness,¹⁴⁻¹⁶ or is not end-to-end and requires to combine multiple components and algorithms to work.^{17,53} Comparatively, our proposed method directly outputs 3D and topological structures of drug-like molecules, without the need for additional atom placement or bond order inference. In fact, to our knowledge, we are the first to apply autoregressive 3D graph generative models to the problem of generating drug-like molecules with 3D structures. The results show that the model is capable of generating chemically correct, conformationally valid, and druglike molecules as output.

We propose a series of techniques to make the model work well for drug-like molecules. Local coordinate systems are introduced to enforce rotational equivariance while ensuring the model’s expressiveness (Section 2.3); SoftMADE is used to address the problems during the fitting of atom position distribution (Section 2.6); Valence and hybridization state are explicitly considered to improve the quality of local structures (Section 2.6); Errors (or noise) are intentionally added to the input so that the model can learn to correct them (Section 2.7); Ring-first traversal is introduced to generate “expert trajectories” (Section 2.7).

Together, those methods have contributed significantly to the model performance. We also developed techniques to reduce the requirement of computational resources. A hierarchical node clustering method is used to enable pooling and unpooling on molecular graphs (Section 2.5), reducing the memory requirement on training and enabling the inclusion of hydrogen atoms during generation. Optimizations have been applied to accelerate the generation process (Section 2.10).

Due to its end-to-end nature, the L-Net can be conveniently combined with a variety of techniques to address different design problems in drug discovery. For example, our method can be directly combined with reinforcement learning methods, such as policy gradient or MCTS, to enable objective-oriented molecule generation in 3D space, including structure-based docking objectives. As a demonstration, we combine L-Net with MCTS to test its ability in designing potential inhibitors against ABL1. The result shows that the model is able to generate molecules with a similar interaction mode and a similar predicted binding affinity within the pocket as known inhibitors, such as that shown in Figure 20 f. Based on the results, we believe that the potential of the proposed method is promising for the application in structure-based drug discovery.

Although the performance of L-Net is promising, we note that it does have limitations. Most notably, L-Net is trained using 3D structures generated from RDKit instead of crystallographic data, which is in theory more accurate. There are several challenges in using crystallographic data to train our model. The first one is that the size of data is more limited compared with automatically generated data, especially for drug-like molecules. A potential solution to this problem is to first train on a large artificial dataset generated using RDKit and then fine-tune the model on a crystallographic dataset. The second problem is that the crystallographic conformation of small molecules represents only one conformation (likely the one close to the global energy minimum). However, in many cases in drug discovery, instead of requiring the model to strictly generate conformations close to global energy minimum, we may want a diverse set of conformations to choose from. A likely solution to this

problem is to use molecular dynamics to augment the crystallographic dataset. We left those explorations to future works.

Acknowledgement

This work was supported in part by the National Natural Science Foundation of China (Grants 22033001, 21673010 and 21633001), the National Science and Technology Major Project "Key New Drug Creation and Manufacturing Program", China (Grant 2018ZX09711002), and the Ministry of Science and Technology of China (Grant 2016YFA0502303). We thank Juan Xie for helpful discussions about the ABL1 kinase.

References

- (1) Bohacek, R. S.; McMartin, C.; Guida, W. C. The art and practice of structure-based drug design: A molecular modeling perspective. *Med. Res. Rev.* **1996**, *16*, 3–50.
- (2) Wang, R.; Gao, Y.; Lai, L. LigBuilder: A Multi-Purpose Program for Structure-Based Drug Design. *Molecular Modeling Annual* **2000**, *6*, 498–516.
- (3) Yuan, Y.; Pei, J.; Lai, L. LigBuilder 2: A Practical de Novo Drug Design Approach. *J. Chem. Inf. Model.* **2011**, *51*, 1083–1091.
- (4) Yuan, Y.; Pei, J.; Lai, L. LigBuilder V3: A Multi-Target de novo Drug Design Approach. *Front. Chem.* **2020**, *8*, 142.
- (5) Segler, M. H. S.; Kogej, T.; Tyrchan, C.; Waller, M. P. Generating Focused Molecule Libraries for Drug Discovery with Recurrent Neural Networks. *ACS Cent. Sci.* **2017**, *4*, 120–131.
- (6) GÅşmez-Bombarelli, R.; Wei, J. N.; Duvenaud, D.; HernÅandez-Lobato, J. M.; SÅanchez-Lengeling, B.; Sheberla, D.; Aguilera-Iparraguirre, J.; Hirzel, T. D.;

- Adams, R. P.; Aspuru-Guzik, A. Automatic Chemical Design Using a Data-Driven Continuous Representation of Molecules. *ACS Cent. Sci.* **2018**, *4*, 268–276.
- (7) Li, Y.; Zhang, L.; Liu, Z. Multi-objective de novo drug design with conditional graph generative model. *J. Cheminformatics* **2018**, *10*, 33.
- (8) You, J.; Ying, R.; Ren, X.; Hamilton, W. L.; Leskovec, J. GraphRNN: Generating Realistic Graphs with Deep Auto-regressive Models. *arXiv:1802.08773* **2018**,
- (9) Jin, W.; Barzilay, R.; Jaakkola, T. Junction Tree Variational Autoencoder for Molecular Graph Generation. *arXiv:1802.04364* **2018**,
- (10) Li, Y.; Hu, J.; Wang, Y.; Zhou, J.; Zhang, L.; Liu, Z. DeepScaffold: A Comprehensive Tool for Scaffold-Based De Novo Drug Discovery Using Deep Learning. *J. Chem. Inf. Model.* **2019**, *60*, 77–91.
- (11) Pogány, P.; Arad, N.; Genway, S.; Pickett, S. D. De Novo Molecule Design by Translating from Reduced Graphs to SMILES. *J. Chem. Inf. Model.* **2018**, *59*, 1136–1146.
- (12) Skalic, M.; Jimenez, J.; Sabbadin, D.; Fabritiis, G. D. Shape-Based Generative Modeling for de Novo Drug Design. *J. Chem. Inf. Model.* **2019**, *59*, 1205–1214.
- (13) Skalic, M.; Sabbadin, D.; Sattarov, B.; Sciabola, S.; Fabritiis, G. D. From Target to Drug: Generative Modeling for the Multimodal Structure-Based Ligand Design. *Mol. Pharm.* **2019**, *16*, 4282–4291.
- (14) Gebauer, N. W. A.; Gastegger, M.; Schütt, K. T. Symmetry-adapted generation of 3d point sets for the targeted discovery of molecules. *arXiv:1906.00957* **2019**,
- (15) Simm, G. N. C.; Pinsler, R.; Csányi, G.; Hernández-Lobato, J. M. Symmetry-Aware Actor-Critic for 3D Molecular Design. *arXiv:2011.12747* **2020**,
- (16) Nesterov, V.; Wieser, M.; Roth, V. 3DMolNet: A Generative Network for Molecular Structures. *arXiv:2010.06477* **2020**,

- (17) Ragoza, M.; Masuda, T.; Koes, D. R. Learning a Continuous Representation of 3D Molecular Structures with Deep Generative Models. *arXiv:2010.08687* **2020**,
- (18) Mendez, D. et al. ChEMBL: towards direct deposition of bioassay data. *Nucleic Acids Res.* **2018**, *47*, gky1075–.
- (19) Ronneberger, O.; Fischer, P.; Brox, T. U-Net: Convolutional Networks for Biomedical Image Segmentation. *arXiv:1505.04597* **2015**,
- (20) Gilmer, J.; Schoenholz, S. S.; Riley, P. F.; Vinyals, O.; Dahl, G. E. Neural Message Passing for Quantum Chemistry. *arXiv:1704.01212* **2017**,
- (21) Huang, G.; Liu, Z.; Maaten, L. v. d.; Weinberger, K. Q. Densely Connected Convolutional Networks. *arXiv:1608.06993* **2016**,
- (22) Vaswani, A.; Shazeer, N.; Parmar, N.; Uszkoreit, J.; Jones, L.; Gomez, A. N.; Kaiser, L.; Polosukhin, I. Attention Is All You Need. *arXiv:1706.03762* **2017**,
- (23) Thomas, N.; Smidt, T.; Kearnes, S.; Yang, L.; Li, L.; Kohlhoff, K.; Riley, P. Tensor field networks: Rotation- and translation-equivariant neural networks for 3D point clouds. *arXiv:1802.08219* **2018**,
- (24) Anderson, B.; Hy, T.-S.; Kondor, R. Cormorant: Covariant Molecular Neural Networks. *arXiv:1906.04015* **2019**,
- (25) Ingraham, J.; Riesselman, A. J.; Sander, C.; Marks, D. S. Learning Protein Structure with a Differentiable Simulator. 2019.
- (26) Gao, H.; Ji, S. Graph U-Nets. *arXiv:1905.05178* **2019**,
- (27) Bemis, G. W.; Murcko, M. A. The Properties of Known Drugs. 1. Molecular Frameworks. *J. Med. Chem.* **1996**, *39*, 2887–2893.

- (28) Wilkens, S. J.; Janes, J.; Su, A. I. HierS: Hierarchical Scaffold Clustering Using Topological Chemical Graphs. *J. Med. Chem.* **2005**, *48*, 3182–3193.
- (29) Germain, M.; Gregor, K.; Murray, I.; Larochelle, H. MADE: Masked Autoencoder for Distribution Estimation. *arXiv:1502.03509* **2015**,
- (30) Kim, H.; Lee, H.; Kang, W. H.; Lee, J. Y.; Kim, N. S. SoftFlow: Probabilistic Framework for Normalizing Flow on Manifolds. *arXiv:2006.04604* **2020**,
- (31) Bickerton, G. R.; Paolini, G. V.; Besnard, J.; Muresan, S.; Hopkins, A. L. Quantifying the chemical beauty of drugs. *Nat. Chem.* **2012**, *4*, 90–98.
- (32) ArÅžs-Pous, J.; Johansson, S. V.; Prykhodko, O.; Bjerrum, E. J.; Tyrchan, C.; Raymond, J.-L.; Chen, H.; Engkvist, O. Randomized SMILES strings improve the quality of molecular generative models. *J. Cheminformatics* **2019**, *11*, 71.
- (33) Paszke, A. et al. PyTorch: An Imperative Style, High-Performance Deep Learning Library. *Advances in Neural Information Processing Systems*. 2019.
- (34) Kingma, D. P.; Ba, J. Adam: A Method for Stochastic Optimization. *arXiv:1412.6980* **2014**,
- (35) Lam, S. K.; Pitrou, A.; Seibert, S. Numba: A llvm-based python jit compiler. *Proceedings of the Second Workshop on the LLVM Compiler Infrastructure in HPC*. 2015; pp 1–6.
- (36) Polykovskiy, D. et al. Molecular Sets (MOSES): A Benchmarking Platform for Molecular Generation Models. *Front. Pharmacol.* **2020**, *11*, 565644.
- (37) Brown, N.; Fiscato, M.; Segler, M. H. S.; Vaucher, A. C. GuacaMol: Benchmarking Models for de Novo Molecular Design. *J. Chem. Inf. Model.* **2019**, *59*, 1096–1108.

- (38) Sauer, W. H. B.; Schwarz, M. K. Molecular Shape Diversity of Combinatorial Libraries: A Prerequisite for Broad Bioactivity. *J. Chem. Inf. Comp. Sci.* **2003**, *43*, 987–1003.
- (39) Mitternacht, S. FreeSASA: An open source C library for solvent accessible surface area calculations. *F1000Research* **2016**, *5*, 189.
- (40) Schreyer, A. M.; Blundell, T. USRCAT: real-time ultrafast shape recognition with pharmacophoric constraints. *J. Cheminformatics* **2012**, *4*, 27.
- (41) Grant, J. A.; Gallardo, M.; Pickup, B. T. A fast method of molecular shape comparison: A simple application of a Gaussian description of molecular shape. *J. Comput. Chem.* **1996**, *17*, 1653–1666.
- (42) Nishino, R.; Loomis, S. H. C. CuPy: A NumPy-Compatible Library for NVIDIA GPU Calculations. *31st conference on neural information processing systems* **2017**, 151.
- (43) Kynkäänniemi, T.; Karras, T.; Laine, S.; Lehtinen, J.; Aila, T. Improved Precision and Recall Metric for Assessing Generative Models. *arXiv:1904.06991* **2019**,
- (44) Riniker, S.; Landrum, G. A. Better Informed Distance Geometry: Using What We Know To Improve Conformation Generation. *J. Chem. Inf. Model.* **2015**, *55*, 2562–2574.
- (45) Yang, X.; Zhang, J.; Yoshizoe, K.; Terayama, K.; Tsuda, K. ChemTS: an efficient python library for de novo molecular generation. *Sci. Technol. Adv. Mat.* **2017**, *18*, 972–976.
- (46) Xiao, C.; Huang, R.; Mei, J.; Schuurmans, D.; Muller, M. Maximum entropy monte-carlo planning. *Advances in Neural Information Processing Systems* **2019**, *32*, 9520–9528.

- (47) Koes, D. R.; Baumgartner, M. P.; Camacho, C. J. Lessons Learned in Empirical Scoring with smina from the CSAR 2011 Benchmarking Exercise. *J. Chem. Inf. Model.* **2013**, *53*, 1893–1904.
- (48) Chaslot, G. M. J. B.; Winands, M. H. M.; Herik, H. J. v. d. Parallel Monte-Carlo tree search. *Proceedings of 6th International Conference on Computers and Games (CG)* **2008**, *5131*, 60–71.
- (49) Schoepfer, J. et al. Discovery of Asciminib (ABL001), an Allosteric Inhibitor of the Tyrosine Kinase Activity of BCR-ABL1. *J. Med. Chem.* **2018**, *61*, 8120–8135.
- (50) Goddard, T. D.; Huang, C. C.; Meng, E. C.; Pettersen, E. F.; Couch, G. S.; Morris, J. H.; Ferrin, T. E. UCSF ChimeraX: Meeting modern challenges in visualization and analysis. *Protein Sci.* **2018**, *27*, 14–25.
- (51) Maaten, L. V. d.; Hinton, G. Visualizing Data using t-SNE. *J. Mach. Learn. Res.* **2008**, *9*.
- (52) Pedregosa, F.; Varoquaux, G.; Gramfort, A.; Michel, V.; Thirion, B.; Grisel, O.; Blondel, M.; Prettenhofer, P.; Weiss, R.; Dubourg, V., et al. Scikit-learn: Machine learning in Python. *J. Mach. Learn. Res.* **2011**, *12*, 2825–2830.
- (53) Masuda, T.; Ragoza, M.; Koes, D. R. Generating 3D Molecular Structures Conditional on a Receptor Binding Site with Deep Generative Models. *arXiv:2010.14442* **2020**,